CHALMERS

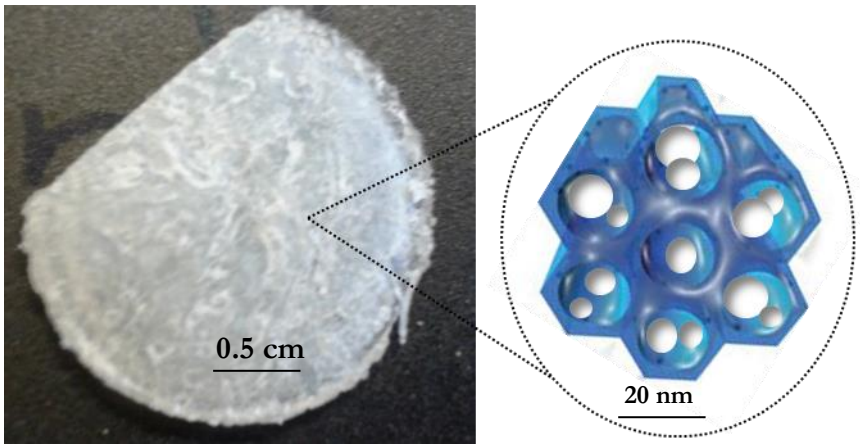

NOVEL ORDERED SYNTHETIC BONE MATERIALS
Implants of the Future

THESIS FOR THE DEGREE OF MASTER OF SCIENCE

ANAND KUMAR RAJASEKHARAN

Department of Chemical and Biological Engineering
CHALMERS UNIVERSITY OF TECHNOLOGY
Gothenburg, Sweden 2014

NOVEL ORDERED SYNTHETIC BONE MATERIALS
Implants of the Future

ANAND KUMAR RAJASEKHARAN

Department of Chemical and Biological Engineering
CHALMERS UNIVERSITY OF TECHNOLOGY
Gothenburg, Sweden 2014

NOVEL ORDERED SYNTHETIC BONE MATERIALS
Implants of the Future
ANAND KUMAR RAJASEKHARAN

Technical report no xxxx:xx
Department of Chemical and Biological Engineering
Chalmers University of Technology
SE-412 96 Göteborg
Sweden
Telephone + 46 (0)31-772 1000

Cover:
Image of the synthetic bone synthesized during the thesis and a schematic of the ordered nanostructure of the synthetic bone showing the arrangement of polymer and calcium phosphate

Printed by:
Chalmers Reproservice
Gothenburg, Sweden 2014

Abstract

Orthopedic implants like hip and knee joints encounter problems with poor tissue integration, corrosion and mechanical instability consequently reducing their lifetime to less than 10 years. This drives a pressing demand for bone substitutes that can achieve true tissue integration, assist regeneration of new bone, and have optimal compressive and fatigue properties with zero toxicity. An intelligent yet challenging solution is to develop a synthetic bone that mimics the chemistry, structure and mechanics of natural bone.

The aim of this thesis was to mimic the ordered assemblies of proteins and minerals (bone apatite) in bone synthetically using in-situ mineralization of apatite in a polymerized liquid crystal (polymer). Lyotropic liquid crystal (LLC) phases like cubic and hexagonal formed by self-assembly of amphiphiles in presence of water have an ordered mesostructure that can be used to mimic biomineralization processes. An earlier work had successfully synthesized nanostructured bone-like apatite within aqueous domains of various LLC gel structures. The present work focuses on synthesizing an ordered nanocomposite by crosslinking a cubic LLC followed by mineralizing apatite within its confined aqueous domains. Small angle X-ray scattering data revealed the meso-ordered structure retention of the mineralized polymer confirming that mineralization did not destroy the ordering of polymer. Morphologically, transmission electron microscopy and X-ray diffraction showed that spherical amorphous calcium phosphates of 8-10 nm in size were formed in the polymer after mineralization which, on aging converted to rod shaped nanocrystalline apatite of 5-10 nm in length. Scanning electron microscopy images showed the surface of nanocomposite to be rough with nanosized apatite crystals embedded uniformly within the polymer matrix. The mineralized polymer showed compressive strength of 1 MPa proving soft which could relate to low density of apatite in the polymer. Cubic LLC polymers failed to control the CaP formation at high precursor ionic strengths leading to mixture of phases such as brushite and monetite along with apatite.

An interesting outcome of this thesis was the ability to control the polymorph of calcium phosphate (CaP) to phase pure apatite at high precursor ionic strengths by varying the LLC phase and pore size. The polymorph of calcium phosphate formed was successfully controlled to bone-like apatite when a hexagonal LLC polymer was used as the matrix with aqueous pore size of approximately 10 nm.

This project has established the possibility of forming ordered polymer-apatite composites with apatite particles well-arranged and ordered within the polymeric matrix at the nanoscale. Further work would focus on improving the implant's mechanical strength and studying its bone-integration and biodegradation *in vivo*.

Keywords: Bone, Lyotropic liquid crysta(LLC), Apatite, Mineralization, Polymer, Composite

Chapter 1: Introduction

Bone-tissue engineering aims at synthesizing functional materials to support a fractured bone tissue or a critical sized bone-defect while simultaneously allowing regrowth of new bone(fig 1.1 a) [1, 2]. A high clinical demand has prevailed for over a century for bone repair and regeneration due to difficulties treating skeletal deformities resulting from congenital defects, slow or non-healing fractures and bone diseases like osteosarcoma and osteoporosis in both young and old population [1, 3]. Progress in development of synthetic materials such as metals, polymers and ceramics as bone substitutes have found a stronghold over the past two decades, popular examples being titanium screws for dental implants, PEEK implants for hip joints and hydroxyapatite granules for filling cranial defects[3, 4]. Synthetic materials must meet vital characteristics to be a good bone substitute like good osteoinductivity and osteoconductivity, osseointegration, load bearing capabilities and non-toxic nature (fig 1.1 b) [5] . These properties can be achieved by tuning the material chemistry, surface topography and by incorporating osteogenic cells (bone forming) and osteoinductive growth factors into the implant. Problems arise when scaffolds dysfunction due to mechanical instabilities and (or) fibrous tissue encapsulation following implantation into the body. Today, orthopedic implants have an average lifetime of up to 15 years and there is yet no reported material on the market that possesses true tissue integration capabilities and optimal mechanical stability without release of toxic byproducts[6]. An intelligent, yet challenging solution to develop the ideal bone substitute is synthesizing a polymeric composite material that mimics the chemistry, structure and mechanics of natural bone.

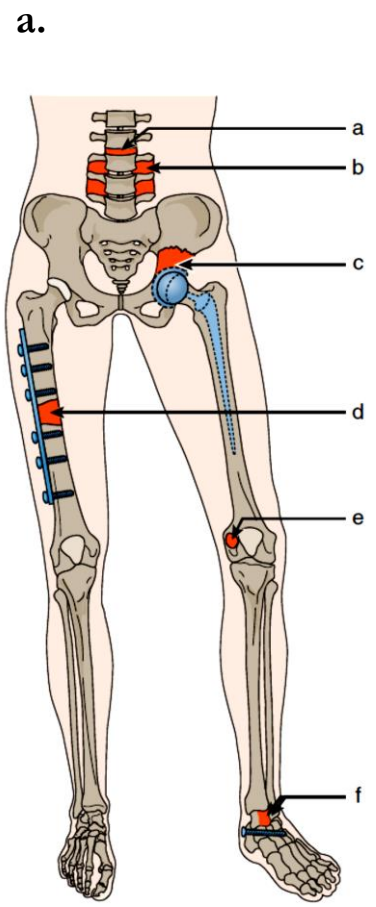

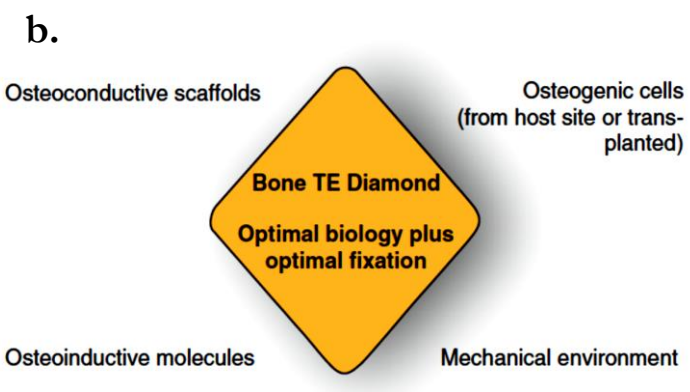

Fig 1.1 (a): Different areas of injuries or fractures**; a &b:** Spinal fusion injury **c:** hip replacement **d:** long bone defects **e:** avascular necrosis **f:** ankle joint defects [5]

(b) The BTE diamond shows the four important factors controlling the development of an ideal bone substitute material [5]

1.1 Understanding Bone: Hierarchical Structure and Mechanics

Bone has a complex, dynamic and hierarchical structure from the macro scale (centimeters) to the molecular scale (angstroms) as shown in fig 1.2. At the highest length scale, bone can be seen as two components, the cancellous bone and the cortical bone while at nanoscale, bone is a composite material constituting inorganic calcium phosphates (CaP) in its apatite polymorph (~50% by vol. or 65-80% by weight) within a protein matrix called type I Collagen (~40% by vol. or 20-30% by weight)[7].

Bone in general has protective layers, the cortical shell covering the inner cancellous core since cancellous bone is soft and contains the bone marrow and numerous blood vessels. From a structural and mechanical perspective, the cortical bone is of primary importance as it constitutes almost 80% of total bone weight. At microscale, the cortical bone has a well-defined architecture consisting of ordered cylindrical structures called lamellae (fig 1.2). The lamellae is a dense arrangement of mineralized collagen fibers arranged as sheets in a regular, ordered and cylindrical fashion wrapped up in concentric layers (3-8 lamellae). These ordered arrangements of fibers are densely mineralized throughout their entire length and circumference. The lamellae can be further broken down to its constituents, an individual mineralized collagen fiber. On analyzing each fibril that make up a fiber, the nanoscale architecture of bone comes into light where ordered arrangement of collagen fibrils (type 1-collagen) hold together nanosized, plate shaped calcium phosphate particles (CaP) giving a highly ordered nanocomposite (fig 1.2) [8, 9].

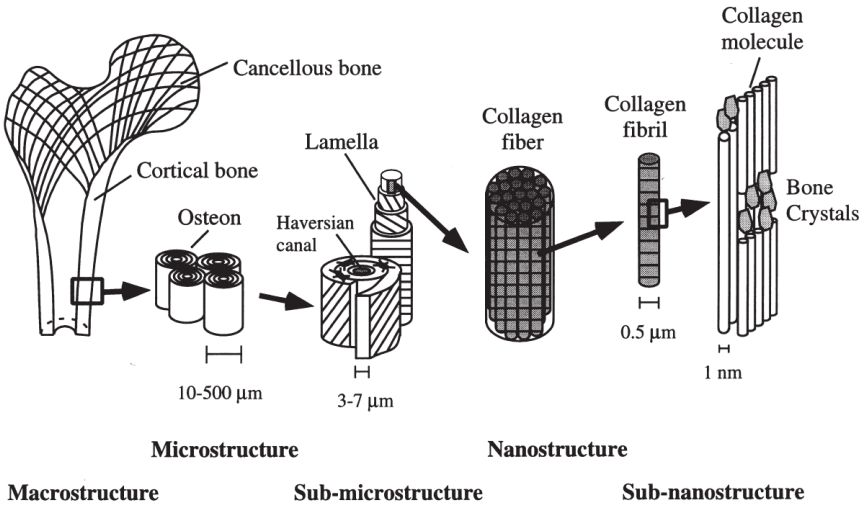

Fig 1.2: Hierarchical structure of human bone showing different levels of structural arrangement at the corresponding length scales [9]

1.2 Collage-Mineral Arrangement in Bone

Collagen mineralization is a biologically controlled deposition process where minerals first grow into gap zones of the staggered arrangement of collagen fibrils with their c-axes parallel to the collagen fibril axis (fig 1.3 a). Individually, a fibril measures 200-300 nm in length and 1.5nm in diameter and is separated by a gap of approximately 35 nm which provide locations for mineral deposition. The mineral adopts a flat, plate like, crystal morphology with dimensions of 50nm in length and 35 nm in width and is aligned parallel to each other along the length of each collagen fibril. The crystals occur at regular intervals with an approximate repeat distance of 67nm which corresponds to the distance by which adjacent collagen fibrils are staggered. These confined

spaces provided by the collagen molecules constrain crystal growth forcing the crystal to fuse into larger plates and squeeze into gap zones of the collagen network thereby producing a compact mineralized fibril network. The last part is the surface mineralization of the fibrils known as intrerfibrillar growth. The organic macromolecular network of collagen and other non-collagenous proteins control and regulate the mineral size, shape and polymorph during the mineralization process [9, 10]. Fig 1.3 (a) shows a schematic impression of the arrangement of staggered collagen fibrils and the location of mineral deposition with respective scale mentioned. Fig 1.3 (b) shows real life SEM image of the cortical section of rat calvaria (skull cap) where highly mineralized and ordered fibers arrangement can be observed. Fig 1.3 (c) shows a modulus vs strength plot of different biological and synthetic materials. It is evident that cortical bone (shown in red) manages to bring in a neat compromise between the toughness of collagen and stiffness of calcium phosphate to obtain a well-balanced composite.

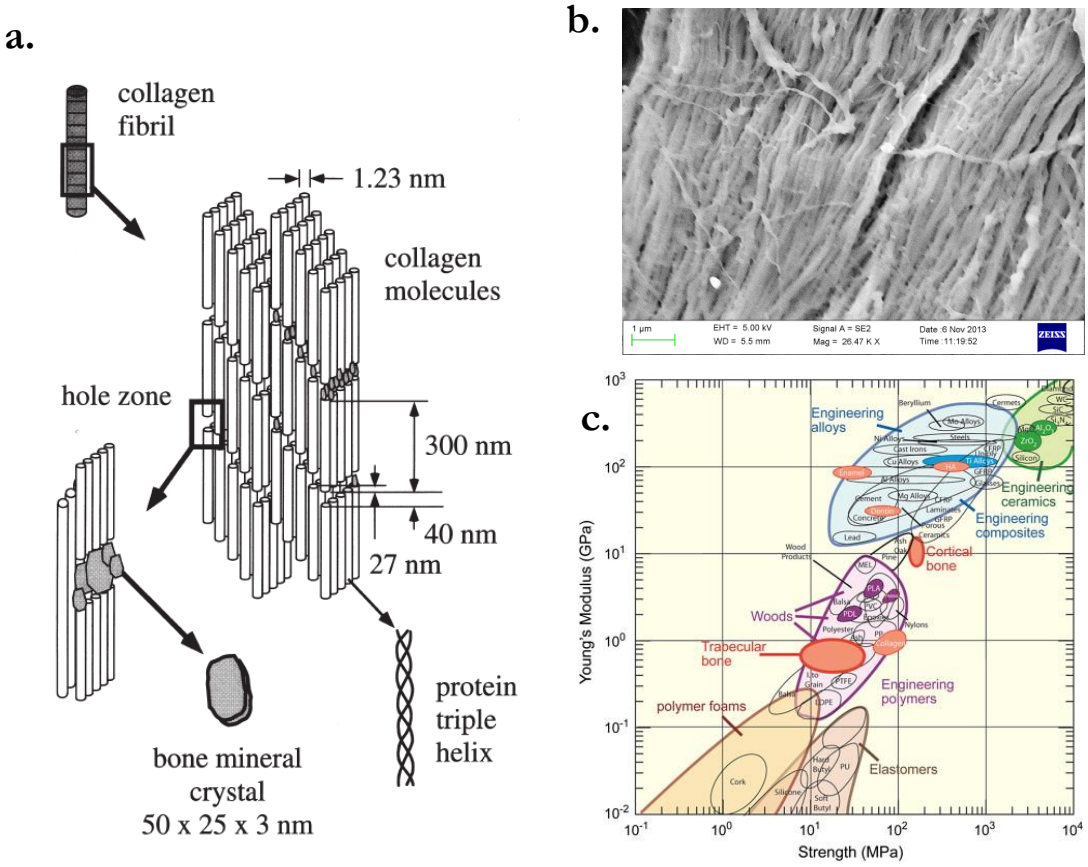

Fig 1.3 (a): Schematic of the ordered arrangement of collagen fibrils and gap zones showing the deposition and growth of apatite minerals [9]**. (b)** A SEM image of a section from rat calvaria (skull cap) showing parallel and densely mineralized collagen fibers (scale: 1μm). **(c)** Graph showing the differences in modulus vs strength of bone compared to synthetic materials[11]

1.3 Mimicing Biomineralization in Synthetic Polymers

Synthetically recreating such a complex and hierarchical tissue like bone is a major challenge and numerous studies have investigated the possibility by utilizing tissue engineering strategies on polymeric scaffolds or *in vitro* mineralization of collagen fibers, however a good biomimetic composite remains to be developed that can mimic the chemistry, structural arrangement and mechanical properties of bone [2, 12]. An interesting route to mimic the structure and

composition of bone is to synthetically recreate biomineralization mechanisms of bone within a polymer. Bone-mineralization is primarily controlled by three factors; confinement, super-saturation and controlled precipitation within the collagen network [13-15]. In addition the ordered arrangement of the collagen fibers ensures that the minerals are monodisperse in size, uniformly distributed and evenly spaced from each other throughout the entire composite. In order to form a fully structured composite an interesting route is to mimic this biomineralization process in an ordered soft polymeric matrix. The predicted requirements of such a polymer are:

a. Confinement: A macromolecular network that has repeating, ordered and confined domains for the crystallization of nanocrystalline bone-apatite
b. Hydrophilic: The polymer must be hydrophilic in order to facilitate in-situ precipitation of calcium phosphate nanoparticles
c. Physical cross-links: The structure must be physically cross-linked that cannot be rapidly degraded within the biological environment
d. Stable under acidic and basic conditions: Due to the possible pH changes during *in vitro* synthesis, the polymer must resist degradation under both acidic and basic conditions
e. Nontoxic: Both polymer and its degradation products needs to be nontoxic

Modern advancements in materials chemistry has introduced a concept called biomimetic morphosynthesis which discusses the possibility of synthesizing inorganic materials such as silica and calcium phosphate that mimic the chemical composition, size, shape and polymorph(in case of crystalline species like calcium phosphate) of natural hard tissues like diatoms and human bone respectively [15, 16]. This method makes use of self-assembled macromolecular networks like proteins or synthetic amphiphiles (surfactants) to act as confined reactors for the formation of complex inorganic materials at ambient temperature and pressure [17-19]. GD Stucky et al have synthesized highly ordered biomimetic silica nanostructures using self-assembled phases of block copolypeptides where the peptides play the role as reactors and templating agents [20]. Of special interest for this study is the biomimetic morphogenesis of bone-like apatite by He et al. where lyotropic liquid crystalline (LLC) phases formed using amphiphilic triblock copolymers were used to template calcium phosphate nanoparticles which exhibited properties similar to bone mineral with appreciable clinical results (further discussed in chapter 2) [21, 22]. The rationale for using lyotropic liquid crystals (LLC) is due to their inherent properties that provide confined nanometric aqueous reactors which can be supersaturated with calcium and phosphate ions. On increasing the pH within these domains, the space restriction drives the formation of nanoscale apatite that resembles the chemistry and morphology of bone-mineral.

1.4 Objectives of this Study

This study aimed to engineer a novel synthetic bone material that mimics the chemistry, nano-structural order and hence mechanical properties of natural cortical bone utilizing *in situ* mineralization of synthetic, cross-linked lyotropic liquid crystals (LLC). Specifically the objectives are twofold:

a. Synthesize cross-linkable LLC structures and study their phase behavior before and after cross-linking
b. Precipitate CaP particles within nanometric aqueous domains of the cross-linked LLC and control the size and polymorph of the CaP particles to form bone-like apatite

Chapter 2: Theory

2.1 Lyotropic Liquid Crystals (LLC) and Applications as Biomaterials

Amphiphilic species like block co-polymers, lipids and proteins may self-assemble into lyotropic liquid crystalline (LLC) structures such as hexagonal and micellar cubic in presence of solvents like water. LLC phases are meso-structures (2-50 nm) having a long range order where the hexagonal arrangement or cubic arrangement of the micelles repeats itself over a long range (fig 2.1)[23-25]. Synthetic LLC phases are being investigated as biomaterials for tissue scaffolds, drug delivery and enzyme immobilization. To quote a few examples, cubic LLC gels synthesized from lipids are investigated as drug delivery agents to the brain and heart and LLC phases are also used to template mesoporous titania and silica for controlled drug delivery to treat bone related diseases like osteoporosis or to eradicate bacterial adhesion on implant materials [26-28]. Furthermore, LLCs are used as nanoreactors to synthesize nanomaterials such as zirconium oxide and calcium phosphate particles for biomaterial coating applications [29, 30].

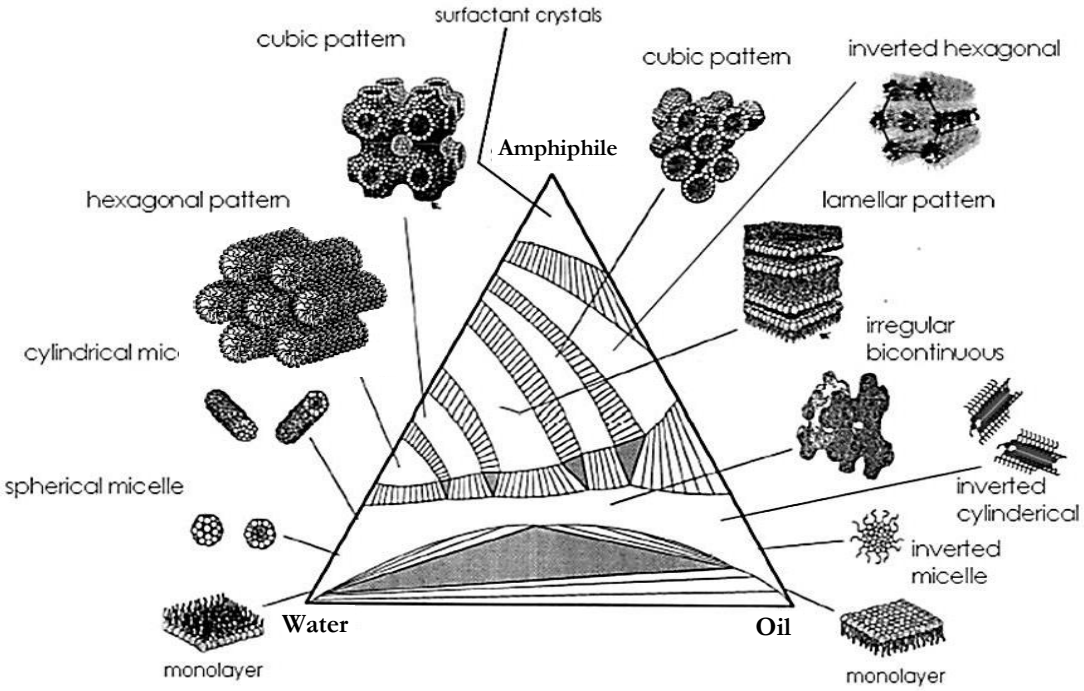

Fig 2.1: A ternary phase diagram showing different lyotropic liquid crystals formed when an amphiphile water and oil are mixed together**.**[25]

2.2 LLC Phases from Amphiphilic Triblock Co-polymers

In the present study, triblock copolymers (trade name Pluronics) were used to form LLC phases with a calcium phosphate precursor solution. Pluronics are amphiphilic polymers with each polymeric molecule consisting of three blocks. Two blocks of polyethylene oxide (PEO) form the hydrophilic head groups (shown in blue in fig 2.2) and a polypropylene oxide block (PPO) forming the hydrophobic tail group (shown in red in fig 2.2). Pluronics are commercially available in different variations as per the chain lengths of each block. For example a particular variation known as Pluronic P123 has a block composition of $(PEO)_{20}(PPO)_{70}(PEO)_{20}$. Pluronics are known to form well-defined lyotropic liquid crystalline phases with water such as hexagonal and has been extensively investigated by Alexandridis et al. and Wanka et al. [31-33]. In the present

study three different Pluronics of varying block lengths have been investigated for the formation of polymerizable LLC phases, further discussed in chapter 3.

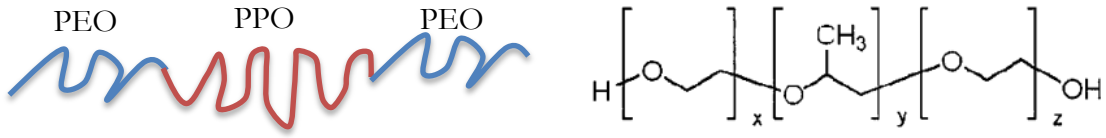

Fig 2.2: The chemical structure of an amphiphilic triblock co-polymer (Trade name Pluronic) used in the present study showing hydrophilic polyethylene oxide (PEO) chains in blue and hydrophobic polypropylene oxide (PPO) chains in red.[21, 33]

2.3 Calcium Orthophosphates (CaPs): Chemistry and Biological Significance

Calcium orthophosphates (CaPs) form the second most abundant inorganic component in biological tissues after silica. The most common biological occurrence of calcium phosphate is apatite which is present in bones and teeth of animals and is a form of CaP chemically and crystallographically similar to synthetic hydroxyapatite [34, 35]. Chemically, CaPs can exist in an amorphous and crystalline state. The crystalline phases of CaP exist in different polymorphs varying in morphology and size although the most thermodynamically stable and biologically significant form of CaP is apatite. Acidic polymorphs such as dicalcium phosphate dihydrate (DCPD) or brushite and dicalcium phosphate anhydrate (DCPA) or monetite also exist in the biological environment such as kidney stone calcifications and dental calculi and some studies even show the presence of brushite as a transient phase during bone mineralization and enamel dissolution [34, 36]. A point of commonality for all types of CaPs is their solubility in only acids. Table 2.1 shows the different types of CaPs, their chemical formula and calcium to phosphate ratio (Ca/P) of each type.

Table 2.1 Different phases of CaP with the respective Ca/P atomic ratios [34, 36]

Name	Formula	Ca/P
Hydroxyapatite	$Ca_5(PO_4)_3(OH)$	1.67
Bioapatite	$(Ca, Na, [\,])_{10}(PO_4, HPO_4, CO_3)_6(OH, F, Cl, H_2O, CO_3O, [\,])_2$	1.33-2.25
Monetite	$CaHPO_4$	1- 1.25
Brushite	$CaHPO_4.2H_2O$	1-1.25
Octacalcium phosphate	$Ca_8H_2PO_4.5H_2O$	1.33
Tricalcium phosphate	$Ca_3(PO_4)_2$	1.5-1.875
Amorphous Calcium Phosphate (ACP)	$Ca_9(PO_4)_{6-x}(HPO_4)_x(OH)_x$	1.2-2.2

2.3.1 Hydroxyapatite (HA) vs Bone-apatite

While chemical and structural parallels can be drawn between bone-apatite and hydroxyapatite, detailed characterization has shown that hydroxyapatite is highly crystalline with stoichiometric proportions of calcium, phosphate and hydroxide atoms occupying a hexagonal close packed lattice with calcium to phosphate atomic ratio of 1.67 (fig 2.3 a). In contrast, bone-apatite is poorly crystalline (fig 2.3 b) and nonstoichiometric, calcium and hydroxide deficient, carbonate substituted and has an average Ca/P ratio of 1.5 [21, 34, 37]. When synthesizing apatite, changes

in temperature and rate of pH increase can produce different transient polymorphs such as tricalcium phosphate and octa-calcium phosphate whose chemistry and formation kinetics are beyond the scope of this thesis.

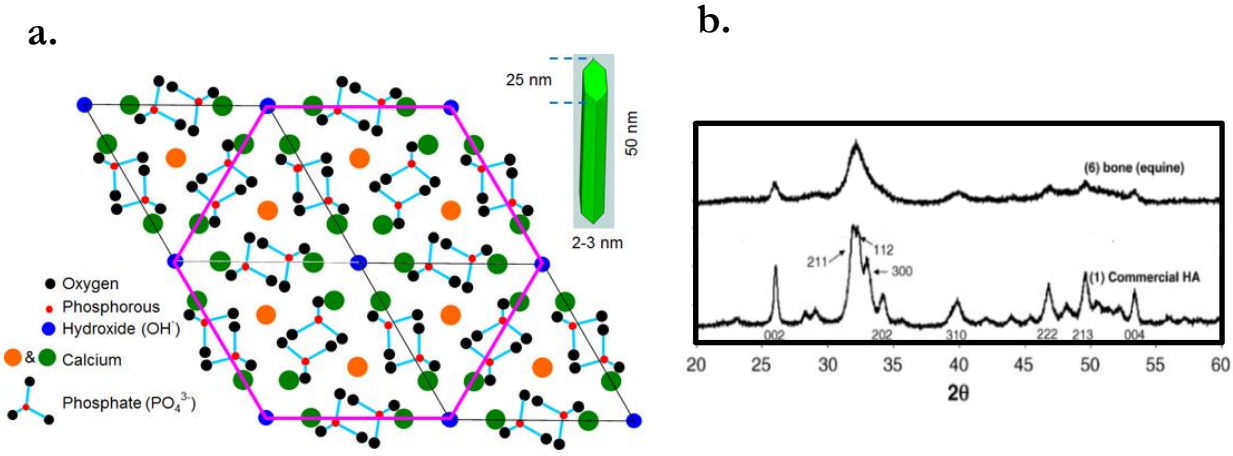

Fig 2.3 (a) Orientations of the different atoms in a hydroxyapatite crystal show a rod-like morphology which tend to gradually convert to a plate like morphology on maturing [38]**. (b)** XRD patterns compare equine bone and synthetic (commercial) HA show broad and low intense peaks for bone indicating the presence of nano-sized poorly crystalline apatite [37].

2.3.2 Amorphous Calcium Phosphate (ACP)

ACPs are conventionally defined as a metastable precursor phase having a distinct spherical morphology and diameter between 10 and 100nm [39, 40] Models predict that ACPs possess short range crystalline domains called 'Posners clusters' (fig 2.4 a) which are similar to crystalline domains of hydroxyapatite (fig 2.4 b) [39, 41]. Studies on bone mineralization of crustacean shells and zebra fish fin have suggested that bone mineralization begins with the formation of amorphous calcium phosphate (ACP) precursor which gradually crystallizes into carbonated-apatite during bone maturation [40, 42]. Numerous studies have shown that during CaP crystallization *in vitro* under moderate super-saturation and neutral pH, ACPs are the first formed species which gradually convert to microcrystalline hydroxyapatite on aging [43, 44].

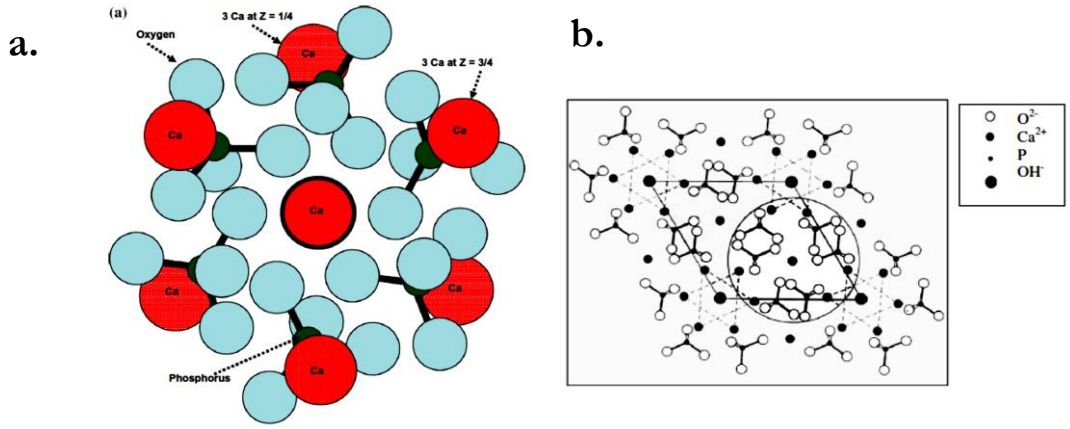

Fig 2.4. (a) Representation of a Posners cluster in ACP sphere [41]**. (b)** Crystalline domains of the Posners cluster shows strong orientations matching that of hydroxyapatite crystal [41]

2.4 Formation of LLC phases

The formation of a LLC is straightforward where the amphiphile and solvents are weighed as per calculated compositions into a container and mixed thoroughly until a homogenous and viscous mixture is formed (at the macroscale 0.5-5 cm) (refer fig 3.4 in chapter 3 for a schematic). At the mesoscale (2-50 nm), the amphiphiles and water self-assemble to form well-ordered LLC structures like hexagonally arranged cylinders or spheres occupying a cubic lattice (see fig 2.1 and 2.9). The long range mesoscale ordering of the phases can be analysed under a microscope or small angle X-ray diffraction (SAXS) for studying their mesoscale structure. Polarized light microscopy (PLM discussed further in section 3) of these gels show clear birefringence in case of a hexagonal or lamellar LLC phase (fig 2.5 a). SAXS can be utilised to determine the meso-ordering in the gels by analysing peak positions from the diffraction patterns (fig 2.5 b)

.

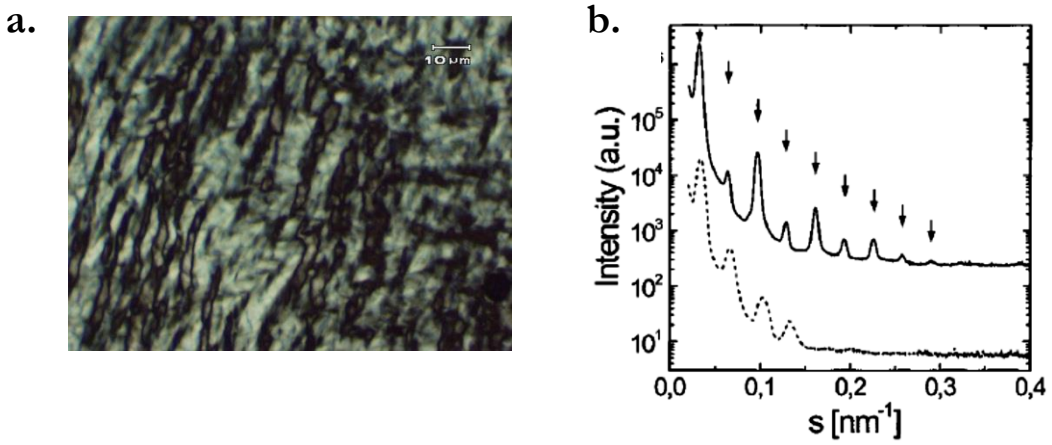

Fig 2.5 (a) Polarized light microscopy image of an LLC gel showing anisotropic behaviour **(b)** SAXS diffractogram of LLC gels shows peaks indicating mesoscale ordering [45]

2.5 Biomimetic synthesis of Calcium phosphate (CaP) within LLC phases

Conventionally, synthetic calcium phosphates like hydroxyapatite has been produced from solution based precipitation where calcium and phosphate ions are dissolved in an acidic medium and the pH of the solution is gently increased where the Ca and P ions combine and undergo a transition through different acidic transient phases eventually converting to stable apatite. A downside to this method is the produced hydroxyapatite lacks properties of bone-apatite in terms of chemical composition and crystallinity. More recently, He et al. applied a reverse hexagonal (H_2) liquid crystal synthesized from amphiphilic triblock co-polymers and aqueous calcium phosphate precursor solution as a medium for controlled mineralization of nanosized bone-like apatite. LLC phases possess ordered, nanometric aqueous domains repeating over a long range where calcium and phosphate ions can be incorporated and on increasing the pH in these domains, the ions react to form spherical nanoparticles of amorphous CaP (ACP) [21]. The LLC arrangement squeezes the CaP particles and assists in controlling the phase and size of the CaP particles as shown in fig 2.6 (a & b). The as prepared ACP particles were used to prepare apatite nanoscrystals through a water mediated aging process. Detailed characterization of the synthesized apatite confirmed the strong similarities it possessed to natural bone mineral in terms of composition, crystallinity, size and morphology.

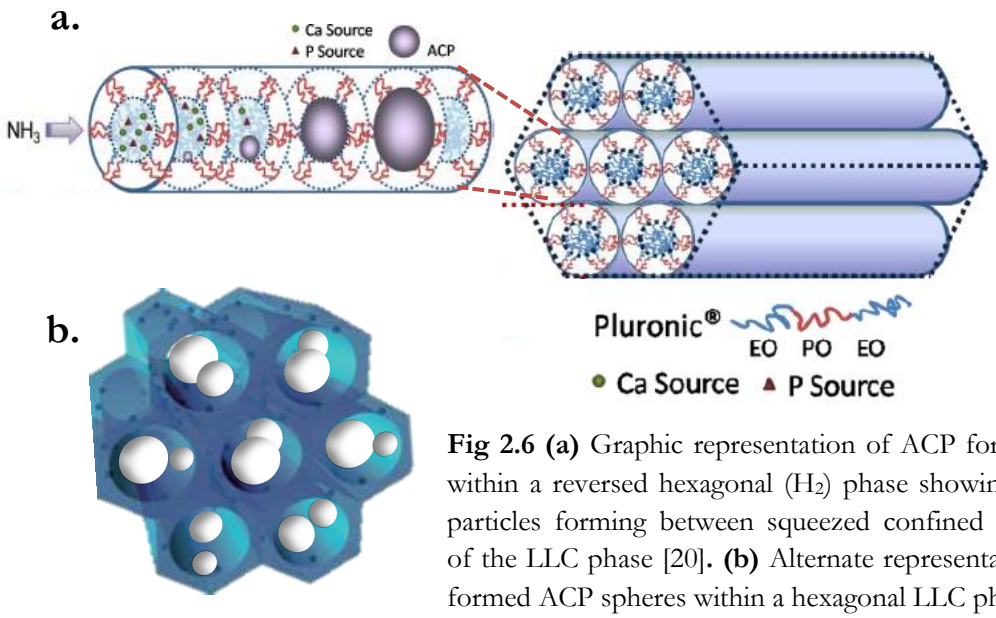

Fig 2.6 (a) Graphic representation of ACP formation within a reversed hexagonal (H_2) phase showing ACP particles forming between squeezed confined regions of the LLC phase [20]**. (b)** Alternate representation of formed ACP spheres within a hexagonal LLC phase.

2.6 Polymerized LLCs as Ordered Polymer Scaffolds

A specific advantage possessed by LLCs are their ability to act as matrices for holding together inorganic materials in an evenly distributed and ordered fashion down to the mesoscale as shown in fig 2.6. However, LLC gels are mechanically soft and flow-able and therefore cannot be used as three-dimensional matrices for the preparation of load bearing bone substitutes. An obvious solution for this is to rapidly crosslink the LLC gels using photons to form LLC polymers. Several routes have been investigated for applying LLCs as templates to synthesize mesosturctured polymers and hydrogels however in most cases the polymers lose their meso-ordered structure once the amphiphilic template is removed. This directed research towards synthesizing polymerizable amphiphiles that can be cross-linked rapidly once it forms a LLC structure with a solvent. Gin et al. and Antonietti et al. have synthesized different crosslinkable amphiphiles and consequently cross-linked respective LLC structures to form mesostructured polymers having ordered geometries like lamellar, cubic and hexagonal [45-48] (fig 2.7 a & b). Polymers having ordered structures with mesoscale arrangement have a wide range of applications from acting as membranes to tissue scaffolds.

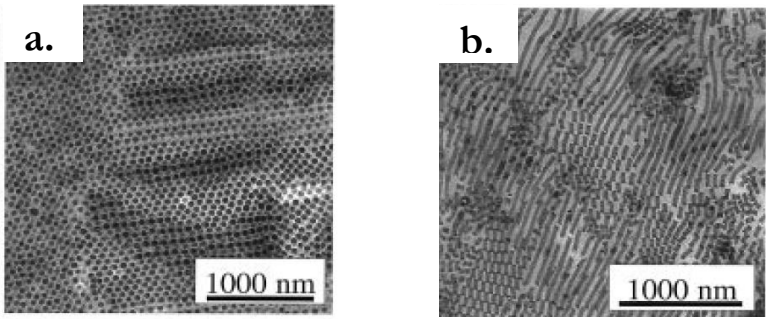

Fig 2.7 (a) TEM image of a crosslinked cubic phase polymer showing ordered and crosslinked pores [43].

(b) TEM image of a hexagonal phase polymer showing worm like cylinders [43].

2.7 Biomimetic approach to synthesize a bone-like nanocomposite

In the present work, LLC phases containing calcium and phosphate ions in their aqueous domains have been cross-linked and mineralized to form ordered polymer-CaP nanocomposites having CaP particles evenly distributed, ordered and well separated from each other within a polymeric matrix as shown in fig 2.8.

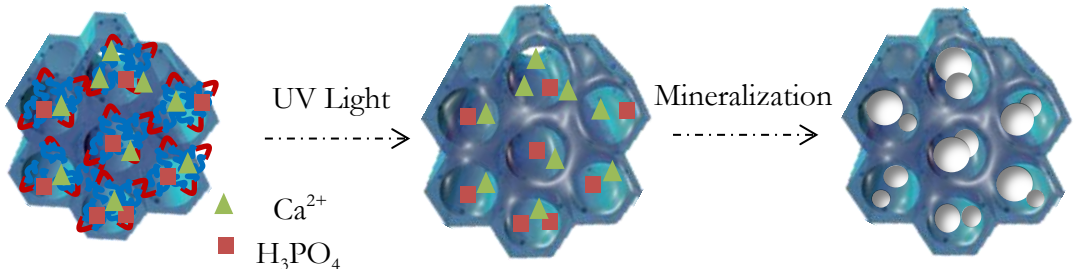

Fig 2.8 Scheme shows the changes in the LLC phase during photon crosslinking and mineralization. The polished junctions represent the crosslinking of amphiphilic molecules while white spheres represent the CaP spheres formed within the nanometric aqueous domains of the LLC polymer

2.8 LLC phases used in this study: Cubic (I_1) and Normal Hexagonal (H_1)

For ease of illustration, the pictorial representations in section 2.7 portray a reverse hexagonal LLC phase as the polymer used for the synthesis of composite. However the present study investigated the micellar cubic and normal hexagonal LLC phases as polymeric matrices for composite synthesis. The main reasons behind choosing such a system are the high water to amphiphile ratio and the absence for an organic solvent to form the LLC phase. Fig 2.9 (left and right) shows the I_1 and H_1 structure and their predicted locations of CaP mineralization.

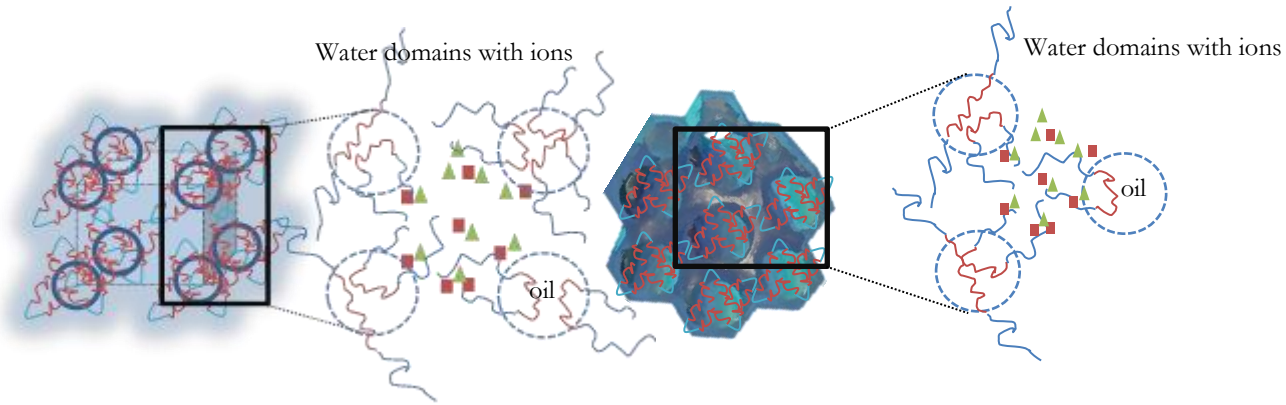

Fig 2.9 (left) A I_1 LLC phase shows the presence of calcium and phosphate ions in the aqueous domains within the LLC. **(right)** H_1 LLC phase shows the presence of calcium and phosphate ions between the voids of each cylinder which are the aqueous domains.

Chapter 3: Materials and Methods

3.1 Synthesis of Polymerizable Amphiphiles

Three commercially available triblock amphiphilic co-polymers, Pluronic F127 ($PEO_{100}PPO_{70}PEO_{100}$), Pluronic P123 ($PEO_{20}PPO_{70}PEO_{20}$) and Pluronic L64 ($PEO_{13}PPO_{30}PEO_{13}$) were chemically functionalized with polymerizable head groups (fig 3.1). All chemicals were purchased from Sigma Aldrich. All the experiments were performed at room temperature (23±1°C) unless specified.

3.1.1 Preparation of Diacrylate modified Pluronic Triblock Copolymers (DA-MF127/L64/P123)

The diacrylate derivative of Pluronic F127/L64/P123, DA-MF127/DA/-ML64/DA-MP123 was synthesized by reacting the amphiphile with acryloyl chloride (Fig 3.1). To a solution of 0.01 mol of the amphiphile in chloroform with triethylamine (TEA), a solution of acryloyl chloride in chloroform was added dropwise at room temperature under N_2 atmosphere with magnetic stirring. The relative molar amounts of TEA and acryloyl chloride are shown in fig 3.1. After 24 h of reaction at room temperature, the reaction products were washed several times with aqueous Na_2CO_3 (5% wt), dried over anhydrous magnesium sulfate ($MgSO_4$), and then the solvent was removed under reduced pressure. The diacrylate derivative of each amphihpile was synthesized with an end product yield of 85-90% respectively[1].

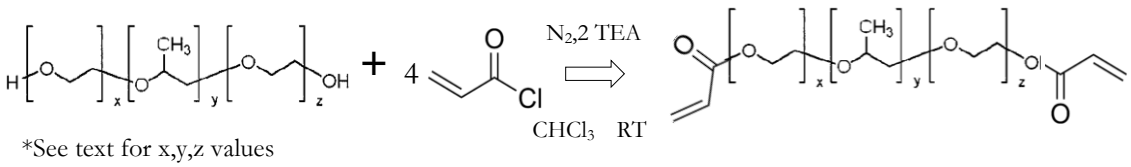

*See text for x,y,z values

Fig 3.1: Reaction Scheme: Synthesis of diacrylate modified Pluronic triblock co-polymer where x y z represents the chain length of each block in a particular polymer

3.2 Calcium phosphate precursor

The aqueous calcium phosphate precursors used for preparation of the LLC phases were prepared by mixing calcium nitrate tetra hydrate ($Ca(NO_3)_2.4H_2O$, 85% phosphoric acid (H_3PO_4) and milli-q water (H_2O) according to a Ca^{2+} ionic strength of 20, 35 and 50 % by weight. The calcium to phosphate (Ca/P) molar ratios of the precursor solutions were 1.67 and 3.34. A high ionic strength represents high concentration of calcium and phosphate ions in the precursor while the Ca/P molar ratio indicates the relative concentrations of calcium to phosphate ions in the aqueous solution.

3.3 The Lyotropic Liquid Crystal (LLC): Modified F127/water LLC system

The phase behavior of F127 and water is well established [32, 49] and fig 3.2 shows the ternary phase diagram of F127, water and butanol. For the present study, the points of interest are pointed out in the respective phase diagram.

[1] Yield = ((amount of product obtained after reaction and purification)/(amount of reactant amphiphile))*100

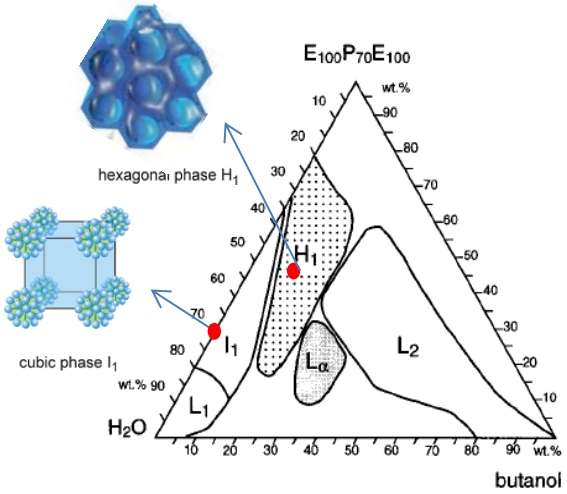

Fig 3.2: Ternary phase diagram of F127/water/butanol system showing different phases formed [49]

Table 3.1: LLC phases studied for the DA-MF127/water/Butanol system and corresponding compositions by weight of each component to form the LLC

Sample name	Phase	DA-MF127 %wt.	Precursor %wt.	Butanol %wt.
F1	Normal micellar Cubic: I_1	35	65	-
F2	Normal hexagonal : H_1	35	50	15

3.4 Modified L64/water and Modified P123/water LLC system

The phase behavior of Pluronic P123 and L64 with water and oil are well established [49, 50] and fig 3.3 (left) shows the ternary phase diagram of L64-water-P-xylene and fig 3.3 (right) shows the ternary phase diagram of P123-water-butanol. For the present study, the points of interest are pointed out in the respective phase diagrams. The H_1 phases of the two amphiphiles were chosen to study the effect of pore size on CaP formation at high ionic strengths, as is further discussed in section 4.4. The recipes for preparing the LLC gel is given in table 3.2 for DA-ML64 and DA-MP123 respectively.

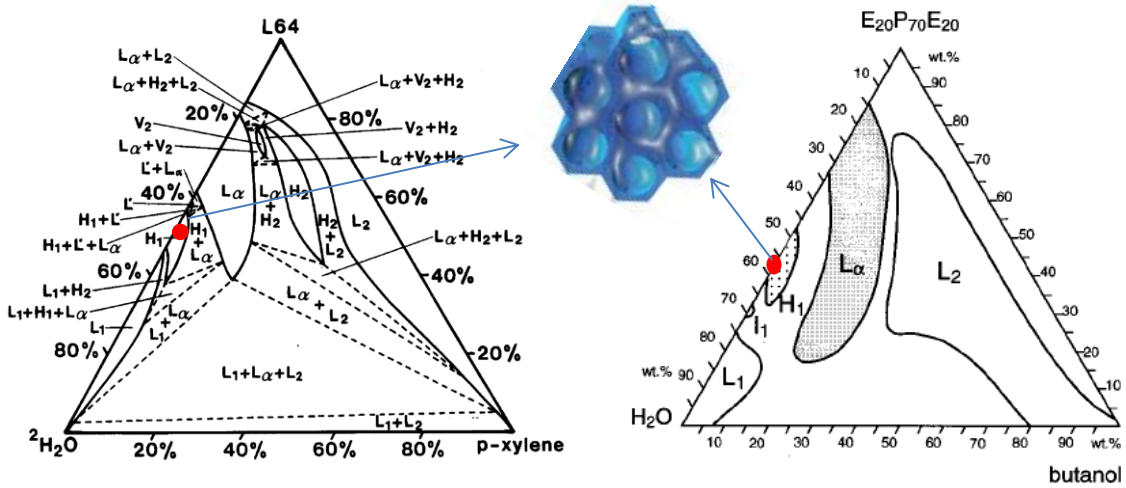

Fig 3.3: Ternary phase diagram of **(left)** L64/water/P-xylene system [50] and **(right)**P123/water/butanol system showing different LLC phases formed [49]

Table 3.2: LLC phases studied for the DA-ML64/water and DA-MP123/water system and corresponding compositions by weight of each component to form the LLC

Sample name	Amphiphile	Phase	Amphiphile %wt.	Precursor %wt.
L1	DA-ML64	Normal hexagonal : H_1	60	40
P1	DA-MP123	Normal hexagonal : H_1	45	55

3.6 Synthesis and Crosslinking the Liquid Crystals: Polymer

The initiator used for UV-crosslinking the LLC was 2-hydroxy 2-methyl propiophenone. The concentration of photoinitiator added was 1wt% of the total block co-polymer composition. To form a LLC gel, the amphiphile, precursor, oil and photoinitiator were mixed as per compositions mentioned in table 3.1 and 3.2. The components were mixed thoroughly using a spatula to form a viscous and homogenous gel. The gel was then transferred into a cylindrical mold and crosslinked under UV-light ((90W lamp, λ = 252 nm) for 10 minutes to form a rubbery polymerized liquid crystal (polymer). The cross-linked LLCs will be referred to as polymers hereafter for example, a I_1 polymer is a polymer synthesized from a micellar cubic LLC gel and H_1 polymer is synthesized from a normal hexagonal LLC gel.

3.7 Synthesis of Polymer-Apatite Nanocomposites

The polymers are in principle crosslinked lyotropic liquid crystals (LLC) which possess nanometric aqueous domains containing calcium and phosphate ions (fig 2.9) and the pH within the aqueous domains is between 0.5 and 0.8 depending upon the ionic strength of the precursor used. In order to mineralize calcium phosphate particles in these ordered nanometric aqueous domains, the pH must be increased to 9 or greater. He et al. had mineralized CaP particles using a diffusion controlled reactor in non-crosslinked LLC gels by placing the LLC gel in an NH_3 atmosphere where the NH_3 gas slowly diffuses within the gel thereby increasing the pH of the aqueous domains of the gel and forming CaP particles. For the present study, since the polymers were relatively rigid and contained high concentration of calcium and phosphate ions in the aqueous domains, two different methods were studied to induce mineralization within the polymer, a diffusion controlled (DC) reactor and a mass flow (MC) reactor. The mineralized polymers will be referred to as composites hereafter. It should be noted that a composites will be termed as per their LLC phase and strength of precursor used, example; an I_1_20Ca is a composite synthesized using I_1 polymer and 20wt. %Ca^{2+} precursor solution while a H_1_50Ca is a composite synthesized from H_1 polymer and 50wt. %. Ca^{2+}precursor solution. A synthesis scheme is shown in fig 3.4 (a, b & c).

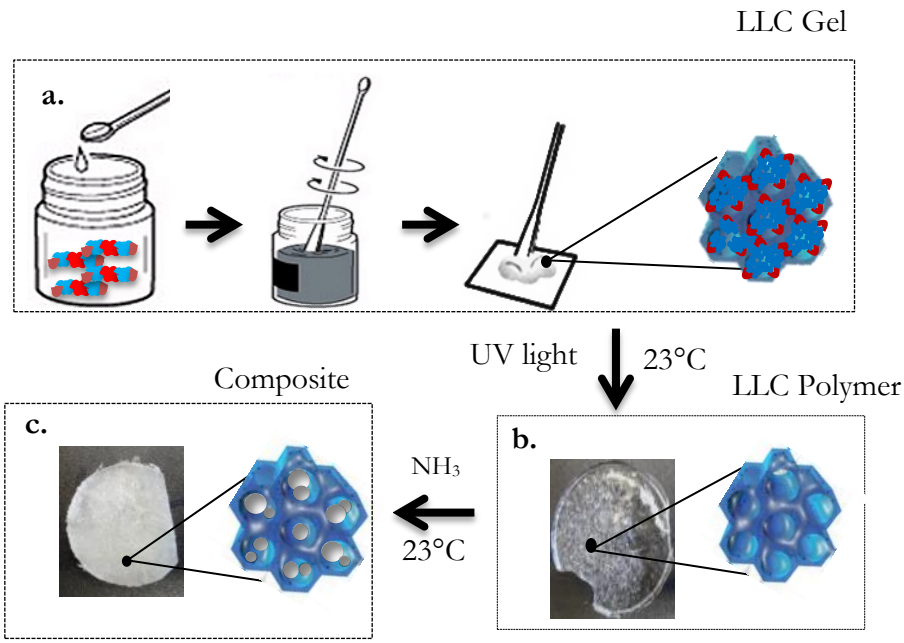

Fig 3.4 Schematic of the synthesis route: from LLC gel to the Polymer -Apatite composite**. (a):** Mixing the modified surfactant and calcium phosphate precursor solution to form a thick paste of Hexagonal LLC gel**. (b):** UV crosslinking the LLC gel to form a polymer **(c):** Passing NH_3 through the polymer to form apatite particles within each aqueous domain of the polymer

In the DC reactor, the samples were placed inside an acrylic box along with a concentrated ammonium hydroxide (NH_4OH) bath (pH=12) (fig 3.5). In a previous work [21], CaP crystallization within LLC gels was achieved by placing the gel in a saturated ammonia atmosphere and the reaction controlled by diffusion. The NH_4OH gradually decomposes to form NH_3 which slowly diffuses into the nanometric aqueous domains of the polymer thereby increasing the pH which induces mineralization of calcium and phosphate ions to form calcium phosphate particles (CaP)

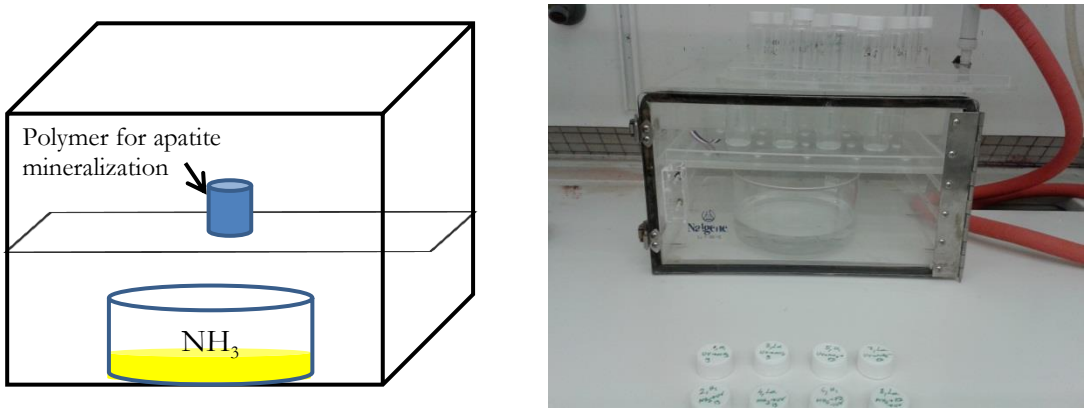

Fig 3.5 (left) Schematic of the DC reactor set-up**. (right)** Image of the DC reactor and samples placed inside

In the MC reactor, the synthesized polymers were placed inside an autoclave connected to a pressurized (7bar, liquid NH_3) ammonia gas flask as shown in fig 3.6 (left). The samples were purged with ammonia gas to increase the pH within the aqueous domains of the polymer for apatite to crystallize and pressure was maintained at 2 bars inside the autoclave. The samples were

exposed to NH_3 for 3 hours with regular monitoring of the pressure gauge (fig 3.6 right). Liquefied ammonia of purity 99.9% was purchased from AGA, Sweden. A stainless steel pressure valve regulated the pressure inside the reactor.

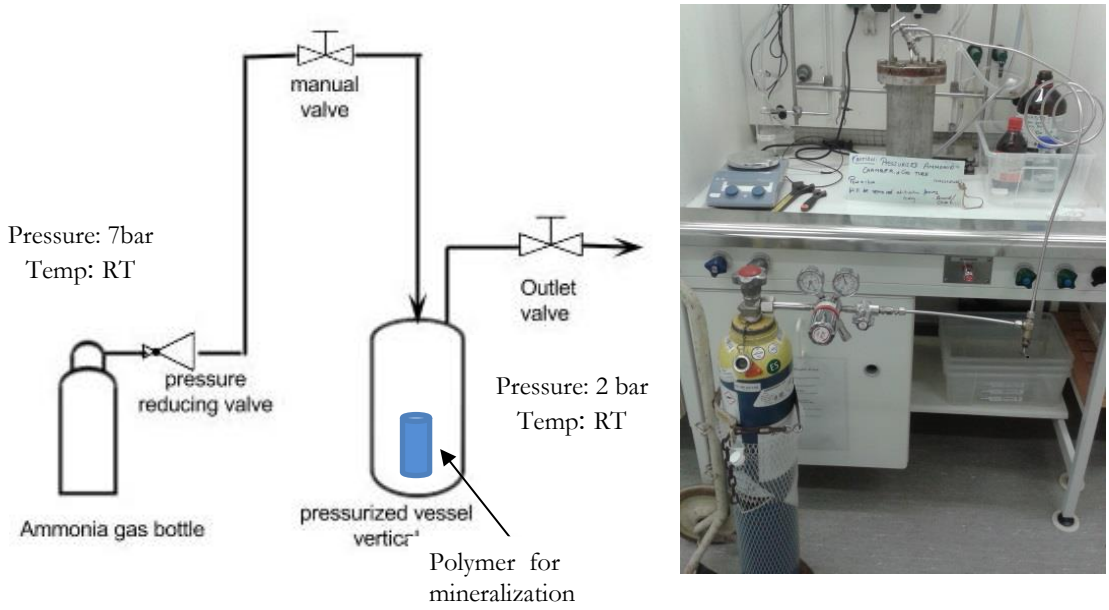

Fig 3.6 (left) Schematic of the reaction set-up**. (right)** Image of the gas bottle connected to pressurized vertical vessel

3.8 Aging of composites: ACP-Apatite Conversion

The composites were aged at room temperature and 60°C for different times (2 days and 6 days) to study its effect on crystallinity of the CaP particles formed.

3.9 Analytical Methods

3.9.1 Polarized Light Microscopy (PLM)

Light microscopy with dual polarized filters can be used to detect presence of anisotropy in materials. Normally, a dual polarized filter will not allow light to pass through which causes the field of view to be dark or devoid of image. However on inserting an anisotropic sample like a LLC gel or crystal changes the state of the polarized light causing light to pass through or scatter displaying a character of birefringence. Conventionally a cubic LLC gel is isotropic in nature which shows no birefringence under a PLM while a hexagonal LLC shows clear birefringence resembling rod-like streaks (see section 2.4, chapter 2 and section 4.1, chapter 4 for representative images).

3.9.2 Small Angle X-ray Scattering (SAXS)

SAXS is a tool primarily used to evaluate structural information of materials at the mesoscale (2-50nm). A beam of high energy X-ray is pointed towards the sample at low angles (<10°) and the scattered X-ray patterns are studied which yields data relating to structural periodicity and pore information of the material in question (fig 3.7). Moreover, the distance between different SAXS diffraction peaks can be used to detect the structure of, for example, if a liquid crystalline phase is

ordered in a hexagonal or cubic fashion [32, 49-51]. In the present study, SAXS was used to study the mesostructure of polymer and polymer-apatite composite and to confirm if the mesoscale ordering was retained following the crosslinking of LLC gel. Table 3.3 shows the adjacent peak ratios of the scattering vector (q) relating to a cubic and hexagonal structure which corresponds to the peaks in a SAXS diffractogram. The scattering vector (q) of the primary or most intense peak can be used to calculate the different geometrical parameters such as pore size and lattice parameter of a particular LLC phase using equations 1, 2, 3 and 4. The SAXS measurements were performed using synchrotron radiation (λ = 0.91Å I911-SAXS beamline at MAX-Lab Lund, Sweden) and a two dimensional Mar 165 CCD detector. The sample was placed in a small slit covered on both sides using a transparent polymeric tape (Kapton) and loaded onto a stainless steel holder. The sample holder was mounted onto an X-ray hutch. Each sample was exposed to high energy X-rays for 120 seconds and the scattering vector (q nm^{-1}) range measured for the samples were between 0.1-4 nm^{-1}.

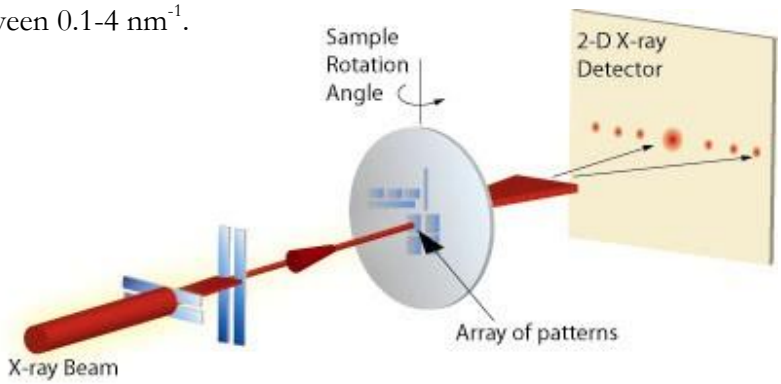

Fig 3.7 Principle of operation SAXS [52]

Table 3.3: Mathematical formulae used for geometrical calculations for data derived from SAXS [32, 53]

LLC Phase	Adjacent peak ratios (h+k+l)	Lattice parameter		Radius of Hydrophobic Domains	
$\mathbf{I_1}$	$1:\sqrt{2}:\sqrt{3}:\sqrt{4}:\sqrt{5}:$	$d_{cub} = \frac{2\pi\sqrt{h^2+k^2+l^2}}{q_{hkl}}$	(1)	$R_{hyp} = 3\frac{f v_p}{\Phi p a_s}$	(2)
$\mathbf{H_1}$	$1:\sqrt{3}:2:\sqrt{7}$	$d_{hex} = \frac{2\pi\sqrt{h^2+k^2+l^2}}{q_{hkl}}$	(3)	$R_{hyp} = d_{hex}\left(\frac{\sqrt{3}}{2\pi}f\right)^{1/2}$	(4)

h,k,l*: Miller indices of each peak in the SAXS diffractogram.*
$\boldsymbol{q_{hkl}}$***:*** *Scattering vector at the corresponding hkl peak*
f*: Volume fraction of hydrophobic domains*
$\boldsymbol{v_p}$*: copolymer volume per molecule (In case of tri-block copolymer)*
Φp*: Volume fraction of amphiphile in the sample*
$\boldsymbol{a_s}$*: Interfacial area of hydrophobic and hydrophilic domain*

3.9.3 Scanning Electron Microscopy (SEM) & Transmission Electron Microscopy (TEM)

Electron microscopy is a direct method for material analysis and imaging. This technique, unlike optical microscopy employs a focused beam of electrons to bombard against the solid sample

and create a highly resolved image. Electrons possess low wavelengths (0.004 nm for a 100 kV accelerating voltage) when compared to visible light (400-700 nm) which helps in giving highly resolved images to the scale of 1nm. In the present study, SEM with EDX and TEM with electron diffraction are used extensively for sample imaging, compositional analysis and crystallographic studies of calcium phosphate particles in the polymer-apatite composite. While both SEM and TEM make use of a focused electron beam to interact with the samples, in SEM electrons are used to scan over the surface of the sample which yields information on sample surface topography. An important requirement for sample imaging using SEM is that the sample must be conductive for electrons. In addition, coupling the SEM with EDX can generate compositional information about the sample. Meanwhile in TEM electrons are used at extremely high accelerating voltages (100-300 kV) to pass through the sample thereby providing a two-dimensional magnified projection of the sample on a fluorescent screen. This working principle of TEM restricts sample size to be extremely thin, usually less than a 100 nm. TEM was used in conjunction with electron diffraction to study the calcium phosphate particle size and crystallinity.

For SEM the samples were cut into thin discs of 5mm in diameter and 1-2mm thickness. All samples were sputtered with gold at a rate of 3nm/min at a plasma current of 10mA and 60 seconds. The imaging was performed on a LEO ULTRA 55 FEG at an accelerating voltage of 5kV. TEM was done on JEOL 1200EX II microscope operated at 120kV. The polymer-apatite composite was first grounded into a fine powder and dispersed in ethanol. A few drops of the dispersion were then dropped onto a lacey carbon coated copper grid followed by evaporation of ethanol.

3.9.4 X-ray Diffraction (XRD)

XRD is a powerful tool that can determine the crystallinity of materials by obtaining their lattice parameters. The technique is to bombard the sample with a rotating X-ray beam which reflects off the sample at certain angles and constructively interfere which is then recorded by the detector as a diffraction pattern. Constructive interference of X-rays from the sample is observed when conditions of Braggs law is satisfied which relates the wave

$$2dsin\theta = n\lambda \quad (5)$$

Where n is an integer representing the order of diffraction peak, θ represents the scattering angle and λ represents the wavelength of the X-ray. The diffraction peaks of all the samples can be compared with the Joint Committee on Powder Diffraction Standards (JCPDS) registry to determine the crystal structure of the material under investigation. The present study utilized a Bruker D8 Advance X-ray diffractometer (Cu-K α1 radiation and λ = 1.54056Å) with a 2θ range of 20-60°, step size 0.050° and data acquisition time of 30 min. XRD was utilized to determine the polymorph of calcium phosphate formed within the composite.

3.9.5 Thermogravimetric Analysis (TGA)

TGA is a tool used to study the thermal stability and degradation of different materials, mainly polymers. The principle adopted by TGA is to heat up the material from room temperature up to 600°C and study the corresponding weight loss. This weight loss vs. temperature curve gives information such as water content in the material, degradation temperature of the polymer and presence of any remaining inorganic content. In the present study TGA was employed for

determining the calcium phosphate mineral content by weight in the polymer-apatite composite. TGA was performed on a Pyris 1 Perkin Elmer thermogravimetry where the sample was heated from 20°C to 550°C at a rate of 10°C/min.

3.9.6 Compressive Strength

The compressive strength of the polymer and polymer-apatite composite was measured on an Instron 5600 universal testing machine. The samples were molded into a cylindrical geometry of 5mm diameter and 5mm in height and placed between the compression plates as shown in fig 3.8. To increase statistical significance, data was recorded for n=10 for each sample variation. The rate of compression was 0.02mm/s and the compressive strength and Young's modulus is defined as the maximum stress at which the sample sustained a 75% strain and the maximum slope of the stress-strain curve respectively [54].

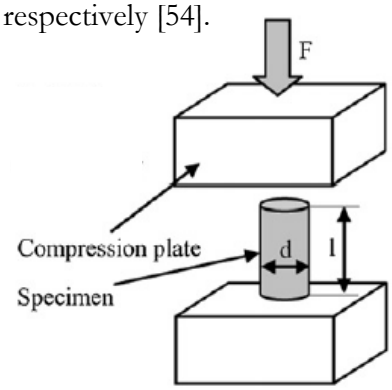

Fig 3.8 Principle of operation compression testing

Chapter 4: Results and Discussion

The aim of this project was two-fold; first: to synthesize polymerizable derivative of amphiphilic molecules and make cross-linked liquid crystal assemblies from them without disrupting their meso-ordered LLC structure. Second: to use the polymers as templating agents and polymer matrix for forming and binding together calcium phosphate (CaP) nanoparticles in their apatite form to produce an ordered synthetic bone-like composite. In view of the multi-sectional nature of this project, the results have been classified as two parts;

1. Synthesis and characterization of cross-linked lyotropic liquid crystal polymers
2. Synthesis and characterization of polymer-apatite composite

4.1 Synthesis and Structure Evaluation of Cross-linked LLC polymers

4.1.1 Investigation of Crosslinking Behavior of LLC gels under UV light

LLC gels prepared as per sample composition F1 was placed under UV light to check if the gels cross-linked. Following UV exposure, the gel (fig 4.1 left) had turned into a rubbery polymeric solid, as shown in fig 4.1 right. The solidification of the gels into rubbery polymers shows direct evidence of the covalent cross-linking of the LLC gel without phase separation of the amphiphile and water. However, it was important to confirm the LLC mesostructure retention of the cross-linked polymer

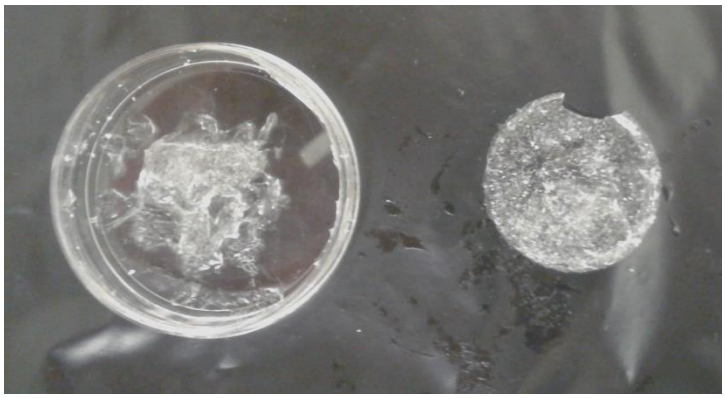

Fig 4.1: Image of a **(left)** freshly prepared I_1 LLC gel. **(right)** gel after UV crosslinking shows a rubbery I_1 polymer

4.1.2 Phase behavior of the Polymer: PLM and SAXS

A series of LLC gels were formed from MF127 and cross-linked under UV-light (see table 3.1) and the LLC gels were analyzed for their phase behavior before and after crosslinking to confirm if the cross-linked polymer retained the LLC structure. Fig 4.2 shows PLM images of a normal hexagonal (H_1) LLC gel before (fig 4.2 left) and after UV-light exposure (fig 4.2 right). The polymer clearly shows the same anisotropic birefringence as the LLC gel suggesting retention of the H_1 structure with long-range order in the polymer.

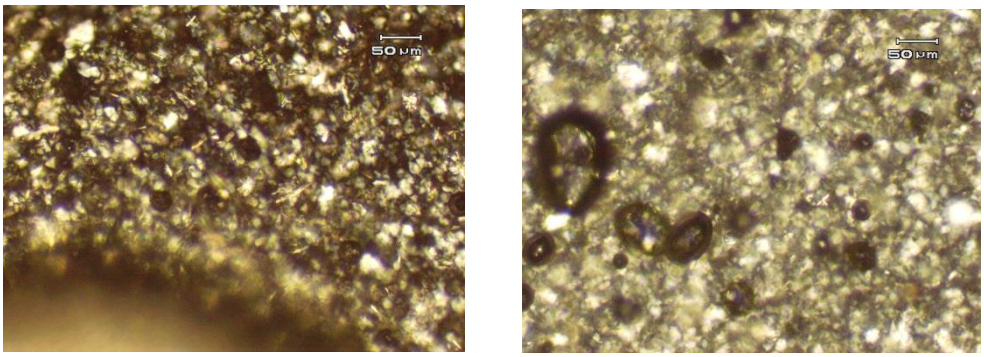

Fig 4.2: (left) PLM image of a H_1 gel shows birefringent rod like features of H_1 phase. **(right)** PLM image of same gel after crosslinking shows the same light scattering

SAXS spectra of the LLC gel and polymer show exactly the same scattering pattern with reflections corresponding to a micellar cubic phase in fig 4.3 (left)[32]. For a normal micellar cubic phase (I_1) at the noted composition as shown in fig 4.3 (left), the type of cubic structure is a primitive cubic cell with spherical to slightly elongated micelles occupying the corners of the cube. The adjacent peak scattering vector (q) ratios are $1:2^{1/2}:3^{1/2}:2:5^{1/2}$ which confirm the I_1 LLC phase in both gel and polymer [32]. An important observation here is that the peak positions have shifted slightly to the left for the polymer when compared to the gel. Considering the reciprocal relationship between lattice spacing and scattering vector (see table 3.3), this effect is due to increase in lattice spacing d_{hkl} of the cube when the LLC crosslinks into the polymer. For the SAXS spectra of the H_1 phase shown in fig 4.3 (right), the adjacent peak ratios of the scattering vector correspond to $1:\sqrt{3}:2:\sqrt{7}$ and similar trends in peak shifts are observed like the cubic spectra [32, 51] .

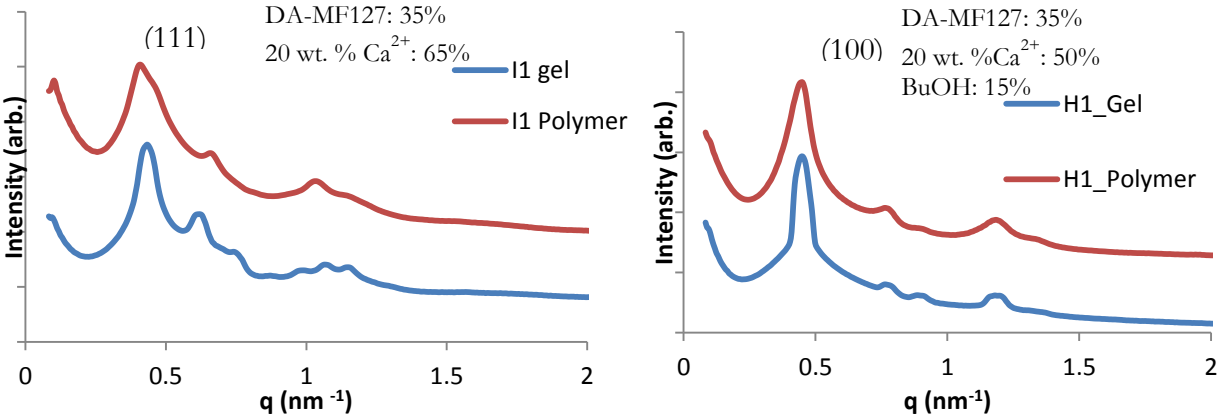

Fig 4.3 SAXS spectra of **(left)** I_1 gel and I_1 polymer and **(right)** H_1 gel and polymer showing LLC structure retention in the polymer after crosslinking

The lattice spacing of the gel and polymer and radius of the hydrophobic domain can be calculated from equations 1 and 3 respectively. On comparing the d_{hkl} of the gel and polymer (see table 4.1), it is observed that the lattice spacing for the polymer is slightly greater than the gel

which is a result of the UV crosslinking. A plausible explanation for this effect; as the hydrophilic head groups' crosslink with adjacent hydrophilic groups, the hydrophobic spheres or cylinders stretch out a little to accommodate the force which in turn increases the size of the hydrophobic domains. This rearrangement of the individual domains creates an average increase of the lattice spacing in the LLC mesophase. Fig 4.4 (left and right) shows a predicted model on how the crosslinking causes the size variation from the gel to the polymer in a cubic and hexagonal phase.

Table 4.1 Geometric parameters calculated for I_1 and H_1 LLC gel and polymer

Phase / Parameters	Micellar cubic LLC (I_1)		Normal hexagonal (H_1)*	
	Gel	Polymer	Gel	Polymer
Lattice spacing (d_{hkl}) nm	25.11	26.18	13.92	14.11

*a_1, r_{hyp} calculations are shown in appendix 1

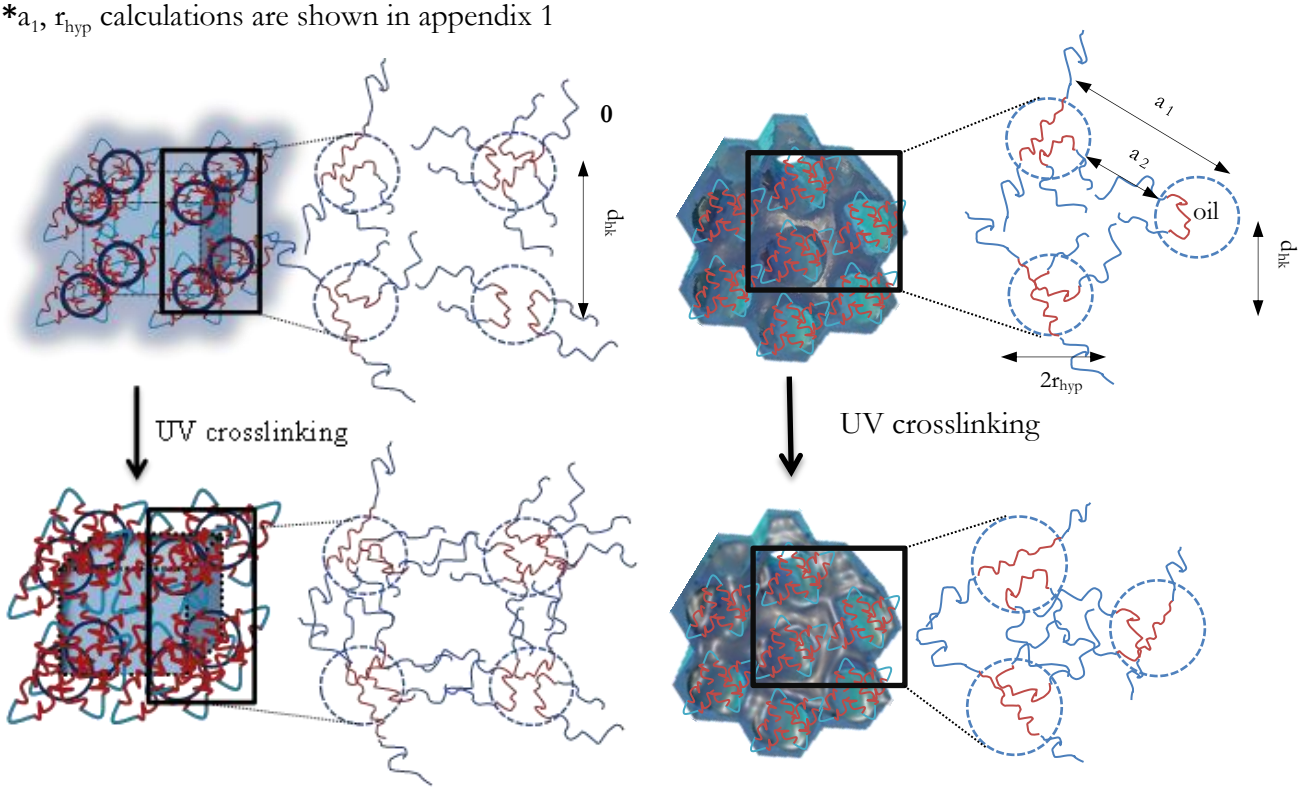

Fig 4.4 Predicted geometric model **(left)** of the I_1 LLC gel and polymer (**right)** and H_1 LLC gel and polymer

4.2 Synthesis of Polymer-Apatite Composites

4.2.1 Calcium Phosphate (CaP) mineralization

CaPs were mineralized within the nanometric aqueous domains of different polymers by purging ammonia (NH_3) gas through the aqueous domains of the polymers to increase the pH in order to induce crystallization of CaPs. Two different methods, a diffusion controlled reactor and a mass flow reactor were used to purge NH_3 through the polymer to produce CaP particles.

4.2.2 Diffusion Controlled (DC)

The microstructure of composites synthesized from this method was visualized using SEM. Fig 4.5 (left) shows a picture of the I_1 polymer and fig 4.5 (right) shows a I_1_20Ca composite. A smooth surface is observed for the polymer while numerous precipitations of micron-sized CaP

particles, characteristic of brushite and monetite are observed on the composite [55, 56]. The same problem kept recurring irrespective of the phase, amphiphile or ionic strength (20, 35 and 50 wt. % Ca^{2+}) used for the synthesis. This method was attempted since it was tried in an earlier work to produce nanosized ACPs within LLC gels with a precursor of low ionic strength which eventually led to higher water content and increased diffusion rates of NH_3. In the present study, the LLC is cross-linked and the ionic strength of the precursor was much greater when compared to the earlier study (ionic strength used in previous study 10 wt.% Ca^{2+} and Ca/P molar ratio= 1.67), which consequently decreases the diffusion rates of NH_3 through the tortuous cross-linked aqueous domains. Moreover, a high initial supersaturation would lower the starting pH in the precursor solution which increases the possibility of forming acidic polymorphs such as brushite. The problem was identified to be the slow increase in pH and a non-uniform pH distribution within the polymer. In view of this, a mass flow controlled (MC) reactor was designed in order to flush pure ammonia into the polymer to achieve uniform homogenous pH increase and therefore homogenous CaP precipitation. A MC reactor would also keep the pressure in the reaction environment constant throughout the entire reaction period.

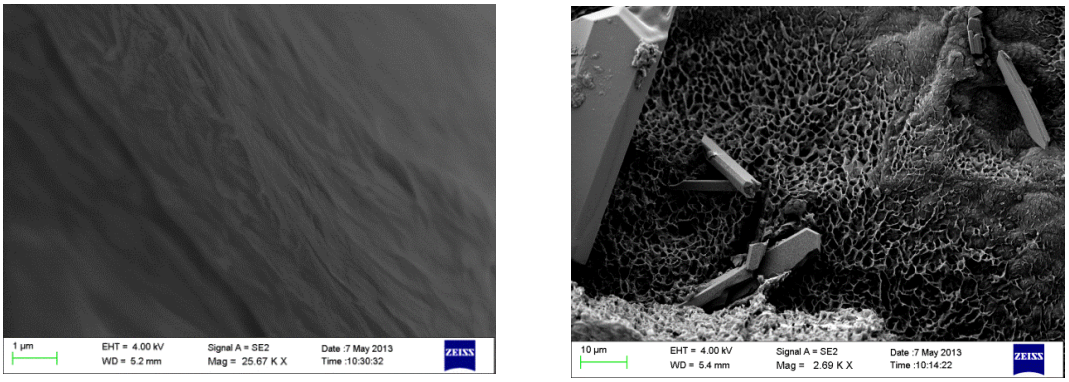

Fig 4.5 SEM images of **(left):** cross-section of the I_1 polymer **(right)** an I_1_20Ca composite showing micron-sized brushite or monetite particles precipitated randomly within the polymer.

4.2.3 Mass flow Controlled (MC)

In the MC reactor samples were initially synthesized at a NH_3 pressure of 0.6 bars to check if micron sized CaP particles formed in the polymer. On SEM analysis of the cross-section of the I_1_20Ca composite as shown in fig 4.6 (a), nanosized CaP particles (EDX spectra in fig 4.6 (b) shows high presence of Ca and P in the sample and corresponds to Ca/P atomic ratio of 1.66, characteristic composition of apatite) were embedded within the polymeric matrix with no micron sized crystals. Since this method showed promising results with respect to apatite mineralization, further experiments regarding all composite synthesis were performed within the MC at higher pressure of 2 bars. The results discussed hereafter will be based on samples synthesized only using the MC reactor.

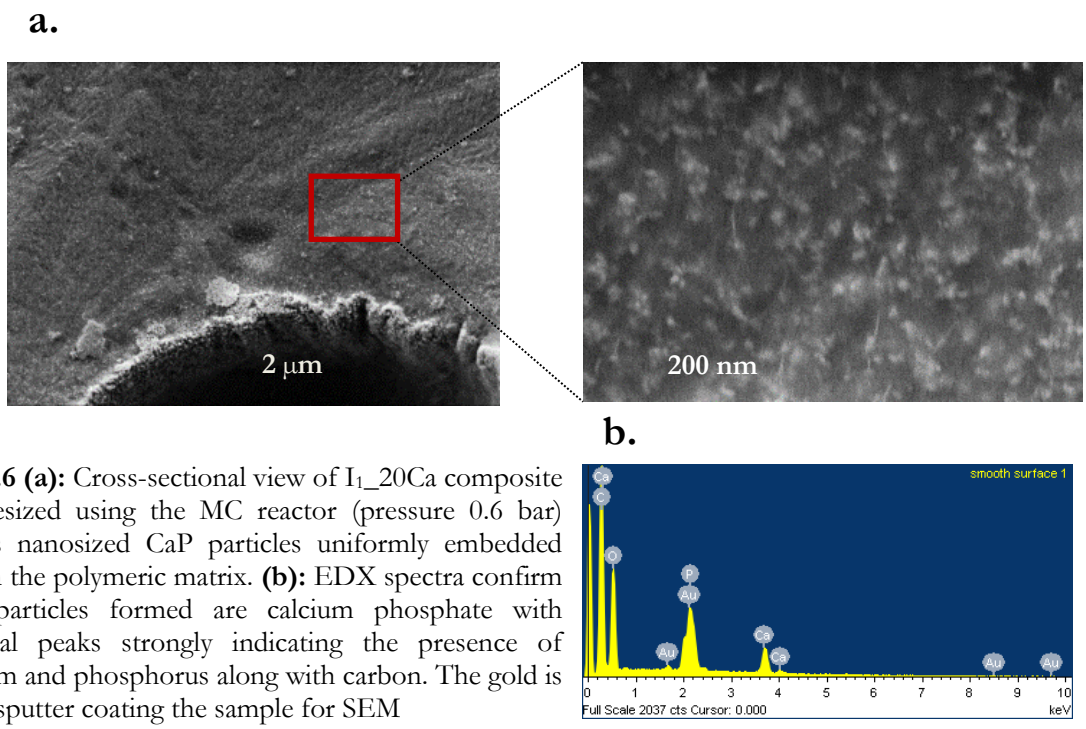

Fig 4.6 (a): Cross-sectional view of I_1_20Ca composite synthesized using the MC reactor (pressure 0.6 bar) shows nanosized CaP particles uniformly embedded within the polymeric matrix. **(b):** EDX spectra confirm that particles formed are calcium phosphate with spectral peaks strongly indicating the presence of calcium and phosphorus along with carbon. The gold is from sputter coating the sample for SEM

4.3 Characterization of Polymer-Apatite Composite

4.3.1 Structure Evaluation of the Composites

The SAXS diffractogram in fig 4.7 (left) displays the scattering pattern of the I_1 polymer and I_1_20Ca[2] composite. The composite clearly show that particle formation has taken place inside the polymer which explains the steep slope observed at lower q values for the composites. This slope is produced as a result of high scattering of X-rays by the CaP particles and thereby loss of contrast. The I_1_20Ca composites formed from MF127 and Ca^{2+} precursor show only the primary peak which has shifted slightly to the left as compared to polymer depicting long range order in the composite, however, other reflections have probably been masked out by particle induced X-ray scattering which makes it difficult to index peaks and calculate any geometrical parameters for the composite. A predicted structure of the I_1_20Ca composite is shown in fig 4.7 (right).

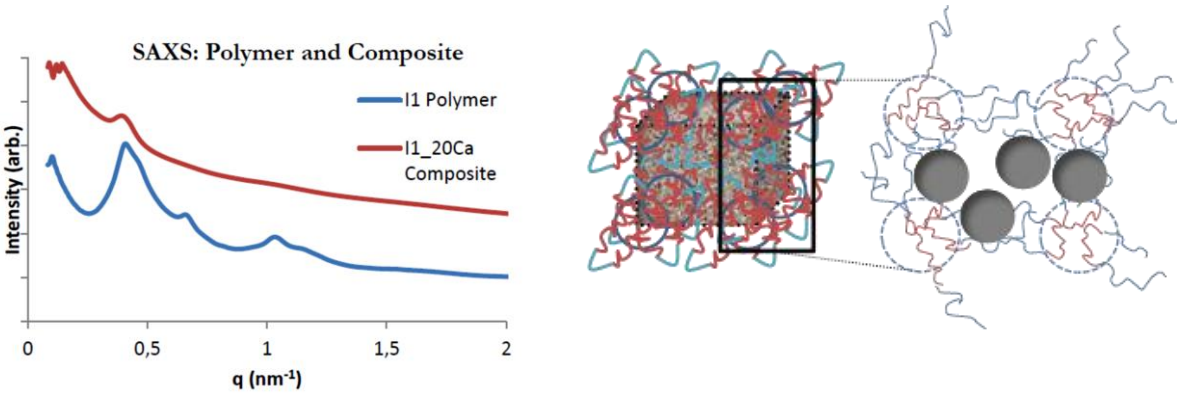

Fig 4.7 (left): SAXS spectra of I_1 polymer and I_1_20Ca composite. (**right**) Predicted locations of calcium phosphate formation in the I_1 polymer

[2] The I_1_20Ca composite discussed from section 4.3 onwards was synthesized in the MC reactor at a NH_3 pressure of 2 bars

4.3.2 Chemical Evaluation of the Composite: CaP Analysis

This section presents the results obtained for composites synthesized using the I_1 polymer and different Ca^{2+} precursor solutions. Fig 4.8 shows XRD patterns of the I_1 polymer and I_1_20Ca[3] composite which indicates the poorly crystalline nature of the polymer (small bump observed at 2 theta=23°) while broad bragg peaks appear in the XRD of composite indicates the presence of small crystalline CaP particles which reinforces the data from SEM images in fig 4.5 (peaks marked with red arrows indicate the hydroxyapatite peaks). Controlling the polymorph of CaP formed is a challenge as multiple metastable phases like brushite and monetite appear as transient phases during apatite crystallization. In order to obtain high apatite mineral content in the composites, precursor solutions of high ionic strengths are required in the I_1 polymer. The next set of studies involved analyzing the type of CaP formed within the composites when the precursor ionic strength was varied between 20 wt. % Ca^{2+} and 50 wt. % Ca^{2+}.

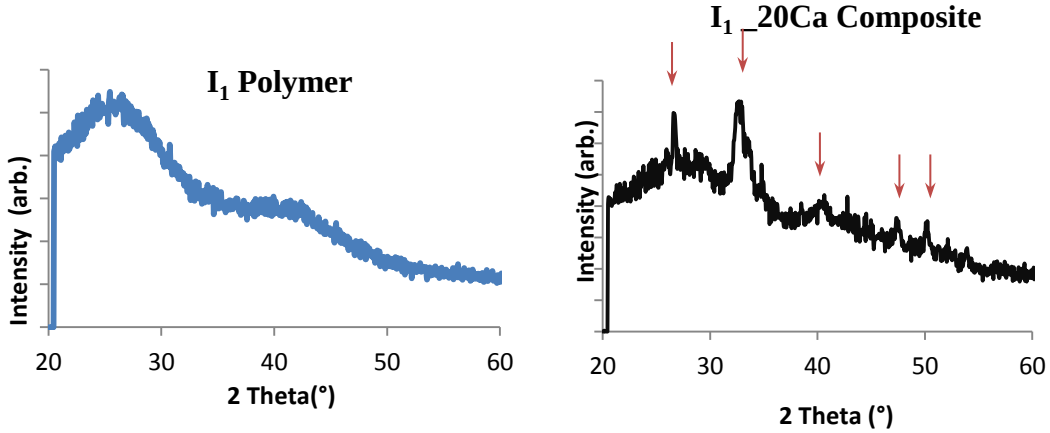

Fig 4.8 XRD patterns of **(left)**: I_1 polymer before mineralization shows amorphous nature except the bump observed at 2 theta = 23° is from the amphiphile. **(right)** The I_1_20Ca composite formed after mineralization shows broad crystalline peaks indicating characteristic of apatite.

4.3.3 Phases of CaPs formed: Effect of Ionic Strength

The ionic strength of the precursor proved to have a major influence on the CaP mineralization of the polymer. Fig 4.9 (left) shows XRD patterns of I_1 composites synthesized from MF127 and precursor solutions of ionic strength 20, 35 and 50% wt. Ca^{2+}. The XRD measurements on the above-mentioned composites were performed immediately after the NH_3 reaction. For an I_1_20Ca composite, the obtained XRD pattern is mostly amorphous with the small bump observed at 2 theta= 24° corresponding to the crysttalinity from the polymer and the sharp peak at 2 theta = 28° (peak marked as 6) could be traces of brushite or monetite still present in the composite. The subtle halo observed at 2 theta= 30° is a characteristic feature of the presence of ACP particles. This observation is further strengthened by TEM images of the composite showing spherical ACP granules (fig 4.9 (c)). As the ionic strength of the precursor is increased to 35 % Ca^{2+} and eventually to 50% Ca^{2+}, ACPs still dominate as the major phase formed within the composite which can be observed in the TEM images (fig 4.9 a & b), however at the same time more and more peaks show up in the XRD corresponding to brushite (Peaks marked 1,2,3 in fig 4.9 left) and monetite (peaks marked 4,5) begin to appear.. Therefore, a mixture of CaP phases form as the ionic strength of the precursor is increased which is undesirable when aiming for a synthetic bone material.

[3] The I_1_20Ca composite was aged at 60°C as per procedure mentioned in section 3.8, chapter 3

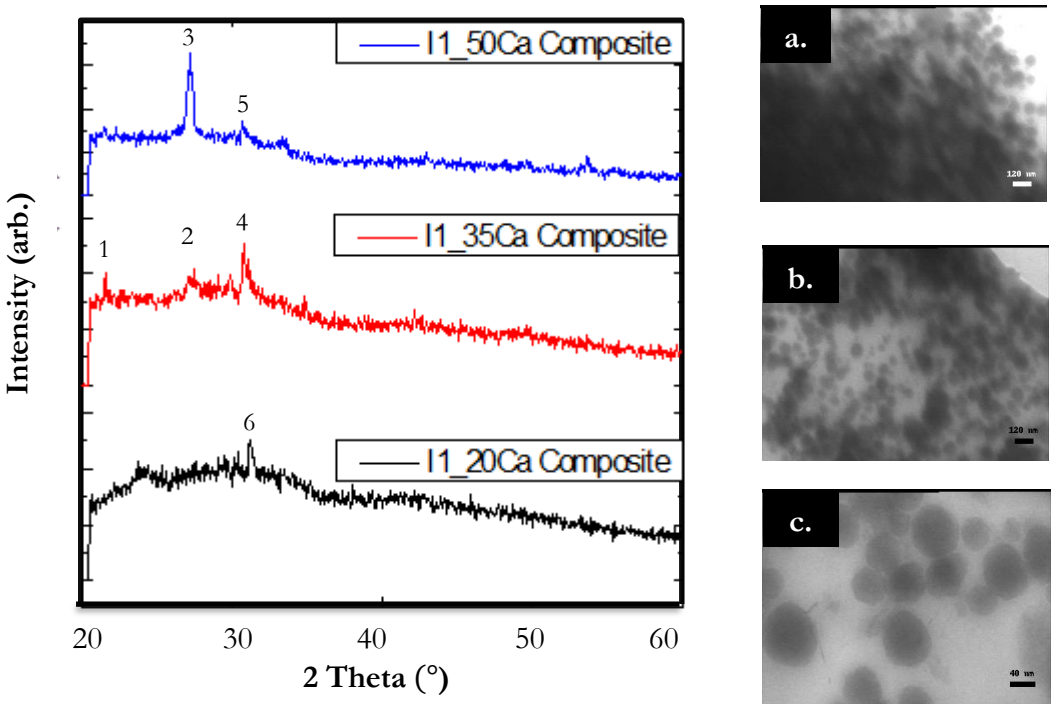

Fig 4.9: **(left)** XRD of Composites measured immediately after NH_3 reaction. **(right)** TEM images of the grounded composite where each image corresponds to the adjacent XRD. **(a)** TEM image of dense ACP granules formed within I_1_50Ca Composite. **(b)** ACP spherical granules formed within the I_1_35 Ca and **(c)** I_1_20Ca composite.

Parallels for the XRD can be drawn by looking at the SEM and EDX data obtained for each composite shown in fig set 4.10. SEM images shows how the composite morphology changes as the precursor concentration is increased from 20 to 50 wt. % Ca^{2+}. Cross-sectional SEM image of composite I_1_20Ca (fig 4.10, a) shows minerals embedded within the composite and the size of the particles are less than a 100 nm as seem from the image. However it is difficult to say if the particles are of amorphous or crystalline nature by looking at the SEM. EDX data on the composite gives an average Ca/P ratio of 2 throughout the cross section which could indicate the domination of ACPs on the composite as seen from the XRD patterns. On increasing the precursor strength to 35% Ca^{2+}, denser mineralization of nanosized CaP particles is observed throughout the cross-section of the composite (fig 4.10, b); however EDX shows a Ca/P atomic ratio between 0.9 and 1.3 at various points of the cross-section indicating presence of acidic polymorphs like brushite and monetite. The SEM results contradict the XRD pattern which can be explained by the localized acquisition of information from SEM as compared to information from a larger portion of the sample using XRD. In contrast to the I_1_20Ca and I_1_35Ca, the SEM image of I_1_50Ca composite (Fig 4.10, c) clearly show large micronsized rod like particles, a classic morphology of brushite particles piercing through the polymeric matrix [55, 57]. EDX measured at point C gives a Ca/P atomic ratio of 0.83, confirming the presence of brushite.

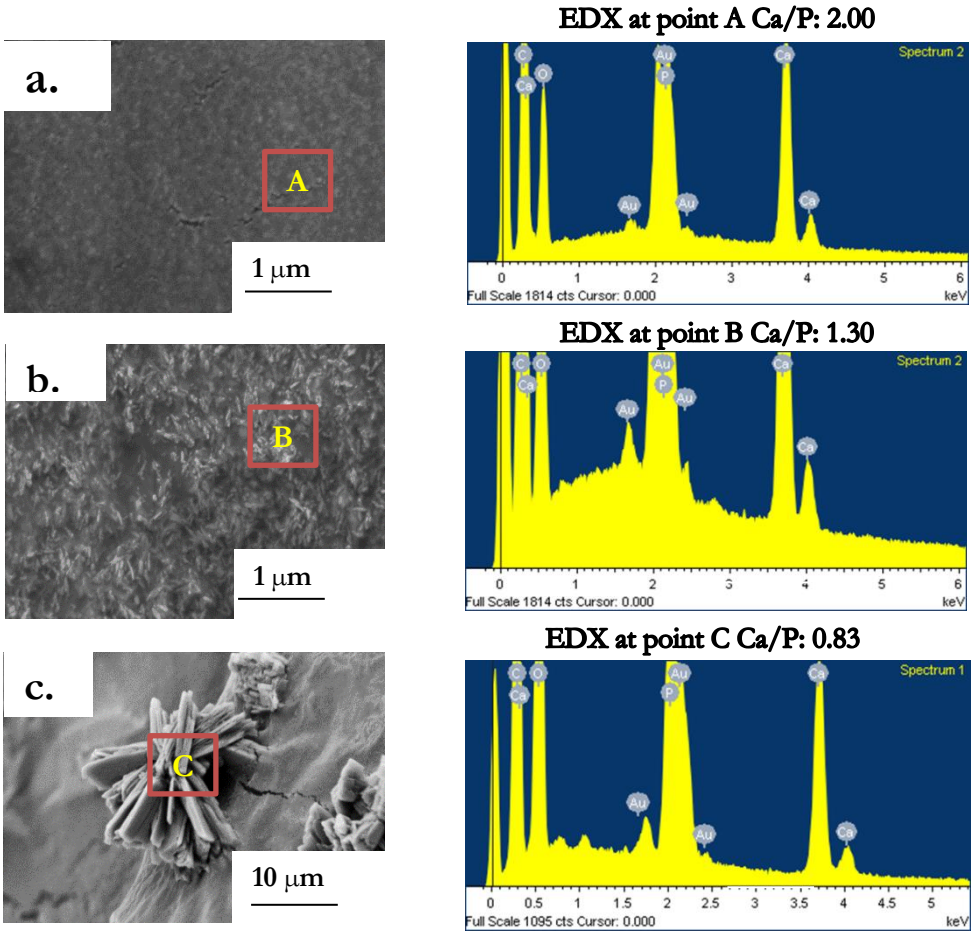

Fig 4.10: SEM and corresponding EDX data of marked areas of **(a)** I_1_20Ca Composites showing uniformly embedded ACP granules within the polymer matrix (scale: 1μm). **(b)** I_1_35Ca shows a bit denser mineralization that I_1_20Ca (scale: 1μm). **(c)** I_1_50Ca shows micron sized brushite particles precipitated unevenly (scale: 10μm). All samples were imaged 1 day after the NH_3 reaction.

4.3.4 Aging the Composites: ACP-Apatite Transformation

ACPs convert to crystalline apatite on aging in the presence of moisture, however a number of factors affect the transformation of ACPs which can be controlled to give poorly crystalline to highly crystalline hydroxyapatite. [21, 44, 58]. He et al. has shown that ACPs produced from liquid crystal based synthesis underwent aging to yield poorly crystalline apatite. As a comparison, conventional water based precipitation yielded polydisperse apatite rods of high crystallinity. In the present study, composites were aged to study the ACP to apatite conversion within the composite.

The I_1_20Ca composites were aged at both room temperature and 60°C to test the ACP to apatite conversion. Fig 4.11 (left) shows the XRD patterns of I_1_20Ca composites before and after aging. On aging at room temperature for a period of 2 and 6 days, broad peaks appear in the XRD pattern of the composite suggesting the gradual transformation of ACPs into poorly crystalline apatite. TEM images (fig 4.11 right, a &b) provide visual proof for the conversion showing rod-like crystalline particles characteristic of apatite. As aging temperature is increased to 60°C the XRD peaks become narrower and the particles further crystallize to form highly crystalline hydroxyapatite rods. TEM images show a rod like morphology for particles aged at

60°C with the electron diffraction showing a mixture of circles and spots indicating strong crystalline nature of the particles (fig 4.11 (right c & d). The XRD of composites aged at 22°C for 6 days strongly indicate similarities with the XRD of equine bone shown in fig 2.3 (a) where both show poorly crystalline apatite character. Moreover, strong resemblances can be observed between the XRD patterns of commercial hydroxyapatite and composites aged at 60°C showing high crystallinity.

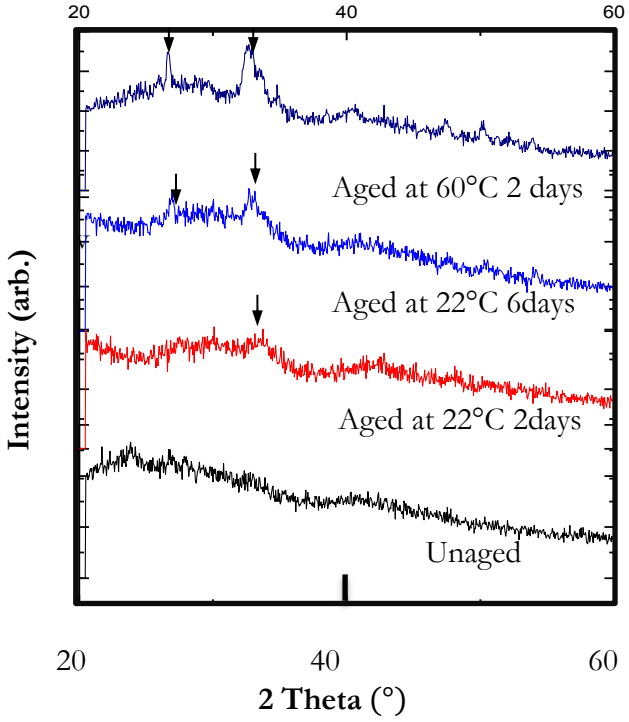

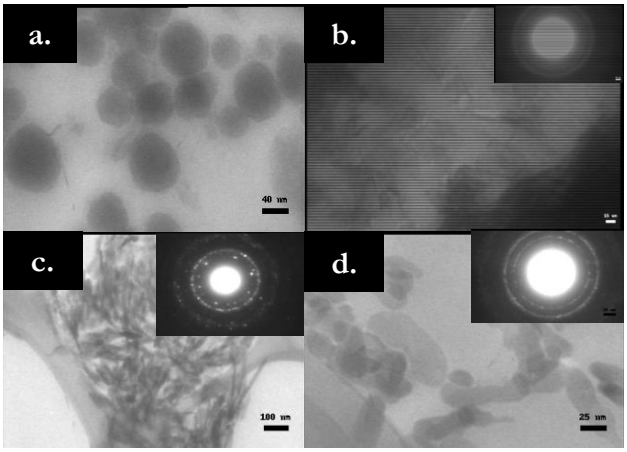

Fig 4.11: (left) XRD patterns of I_1_20Ca composite aged at different time periods and temperature show emergence of bone like apatite within the composite as aging proceeds. **(right)** TEM images confirm the aging process observed from XRD; (a) Unaged (scale: 40 nm) (b) aged at 22°C for 2 days (scale: 15 nm) (c) aged at 22°C for 6 days (scale: 100 nm) (d) aged at 60°C for 2 days (scale: 25 nm)

4.3.5 Brushite/Monetite at high Ionic Strengths: Discussion

The tendency to form acidic CaP polymorphs like brushite and monetite within the polymer is observed to increase as the ionic strength of the precursor solution increases. Fig 4.12 compares the XRD patterns of I_1_20Ca and I_1_50Ca composites which were aged at room temperature for 6 days. The I_1_50Ca composite clearly shows a mixture of phases (peaks marked with stars) like brushite and monetite apart from apatite. Three different hypothesis can be identified which can act individually or together for this anomalous behavior of CaP precipitation in the composite.

1. **pH gradient in the Polymer**

At high ionic strength, the quantity of Ca and P ions are greater and these tend to react rapidly to form CaP particles as the pH of environment changes. This burst precipitation can lead to a pH gradient throughout the length and depth of the polymer. The surface of the polymer that is exposed to NH_3 gas first, begins to experience a rise in pH while the layers beneath the surface experience a slower rise in pH relative to the surface, possibly due to hindrance for NH_3 to penetrate into the polymer by the particles formed on the surface. This leads to certain regions of the polymer to remain at an acidic pH of 3-6 favoring the formation of brushite or monetite.

2. Favorable starting pH for brushite formation

At high ionic strengths, it is not guaranteed that all Ca^{2+} ions will react with PO_4^{3-} ions at a molar ratio greater than 1.3 to form ACP or apatite. Due to extremely low pH (0.50) at high ionic strengths (50 wt% Ca^{2+}), there is a significant amount of HPO_4^{2-} ions which favors the formation of brushite or monetite. A greater Ca/P starting molar ratio might assist the inhibition of brushite/monetite formation.

3. Lack of necessary confinement in the polymer

A third reason which explains this effect is the lack of the required confinement by the cubic LLC polymer to control the polymorph formed. The spherical aqueous domain of an I_1 polymer is approximately 20-30 nm in diameter, which are accessible from all three dimensions and the cross-linked polymer chains are not strong enough to suppress the CaPs to form more stable phases like ACPs and Apatite. Similar effect is observed when CaPs are precipitated in unconfined water based precipitation at high ionic strengths [36] .

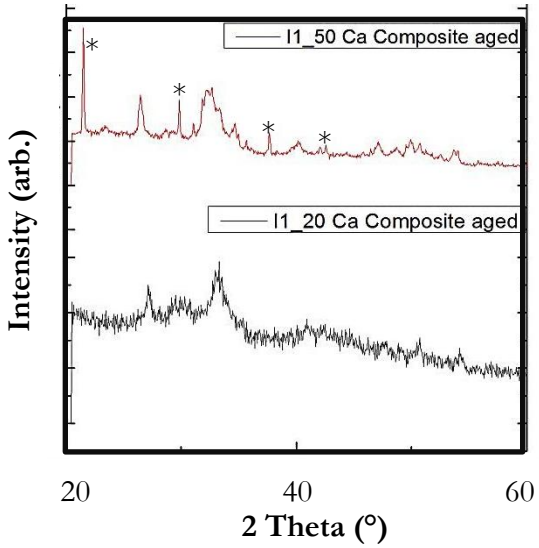

Fig 4.12: XRD diffractograms of aged composites I_1_20 Ca and I_1 _50Ca show phase pure apatite in I_1_20Ca while a mixture of phases are observed in I_1_50Ca

The results from XRD and TEM suggest that for the composite synthesized from a cubic phase prepared using MF127 and 50% wt. Ca^{2+} precursor, the calcium phosphate phases formed are a mixture of ACP, Brushite and Monetite. However, at low ionic concentrations such as 20wt% Ca^{2+}, the CaP formed within the polymer can be controlled to, phase pure, spherical ACP granules with uniform size distribution, converts to poorly crystalline, bone-like apatite on aging. At this juncture, two different routes were selected to proceed with developing the composite where one course was to evaluate the I_1_20Ca composite for thermal and mechanical properties (section 4.3.6 to 4.3.8) while the second course was to control the phase of CaPs to pure ACP or apatite at high precursor ionic strengths within the composite (section 4.4).

4.3.6 Evaluating the mineral content in Composite (I_1_20Ca)

Further analysis was carried out on the I_1_20Ca composite to test the organic-inorganic weight ratio and compressive strength of the composite. The composite was compared against a pure polymer also having the I_1 LLC structure. Thermogravimetric analysis was used to calculate the residual mineral content (by weight %) in the composite. Fig 4.13 shows a TGA of pure polymer

and I_1_20Ca composite. Both polymer and composite have two regions of transition or weight loss. The first weight loss for the polymer starts immediately and saturates at 100°C which corresponds to loss of water from the polymer which comes from the initial addition to form the LLC phase. The second transition for the polymer begins at approximately 350°C and a complete weight loss is observed as the curve saturates a little beyond 400°C. The complete weight loss region suggests the degradation of the polymer into its gaseous components.

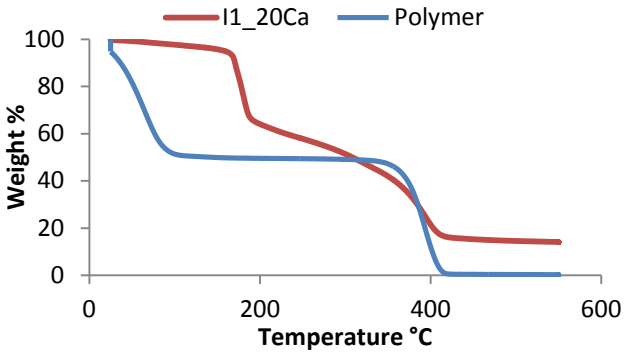

Fig 4.13: TGA of the I_1 polymer and I_1_20Ca composite

The TGA curve of the polymer suggests that the polymer to water weight ratio within the composite is 40:60.

TGA of the composite (fig 4.13) shows two regions of transitions. The first weight loss is observed between 25° C and 200° C; however until 100°C it does not show up as a major transition and the first major weight loss begins at 170 ° C and saturates a little beyond 200° C. This could be attributed to the loss of tightly bound water present as hydrated layer on the ACP mineral particles and the polymer itself. An explanation is the formation of minerals could hinder the mobility of water molecules from the polymer which creates the burst release of water at 170 ° C. There is gradual weight loss beyond 200 °C and saturates a little beyond 400 ° C which suggests a combination of weight loss due to the residual water and polymer degradation. However this needs to be verified by a combination of TGA and FTIR in order to detect the chemical components being released at the different transition points. The most important result from the TGA is the residual weight beyond 500° C which indicates the actual mineral content by weight in the sample. From fig 4.12, approximately 15% of the weight remains beyond 500° C suggesting the inorganic content to be approximately 15% by weight in the composite.

4.3.7 Polymer to Mineral Weight Ratios

The TGA curve of the composite in fig 4.13 implies that the polymer and mineral content is approximately 30% and 15% by weight respectively. The major component present in the composite is water which constitutes up to 40% of the entire weight. This indicates that the amount of polymer is almost double the mineral content present in the composite. The reason behind this observation is the low ionic strength of precursor solution used (20% wt. Ca^{2+}) to synthesize the composite. Fig 4.14 compares the TGA curves of a pure polymer, composites synthesized from 20% and 50% wt. Ca^{2+} and a real bone (rat skull cap). The polymer which is the reference shows zero residual weight at 500 °C while the composites shows corresponding increase in residual weights with increase in precursor ionic strengths i.e. I_1_20Ca shows a residual weight of 14% and I_1_50Ca shows a residual weight of 21%. In both curves the relative

polymer to mineral weight ratio is approximately 1.5 which signifies greater organic content in the composite unlike actual bone which shows at least 75% residual weight and organic to inorganic

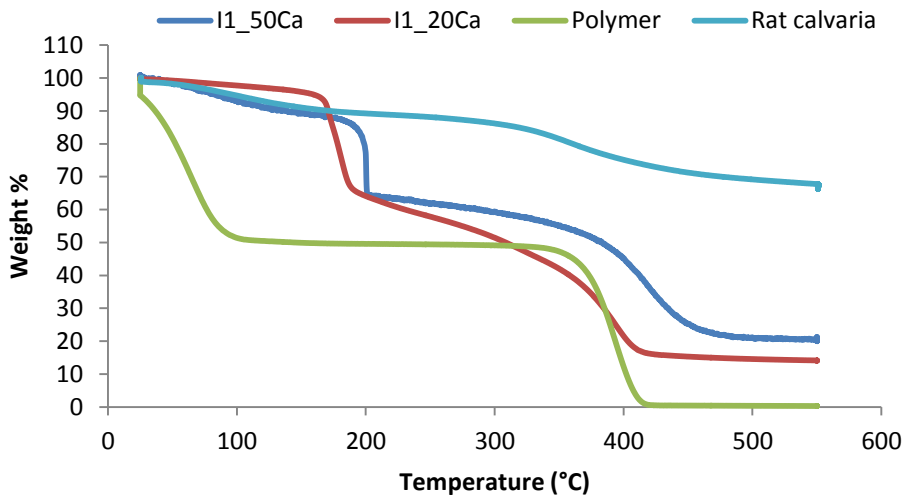

Fig 4.14: Residual weight analysis of different I_1 composites as compared to native rat calvarial bone using TGA

The low mineral content in the composite presents a problem when considering the mechanical properties of the synthetic bone material. Natural hard tissues like bone and dentine vary in the mineral content however the average bone mineral content (BMC) by weight in human bones is about 70% and 85-90% in enamel. The high mineral content is primary contributor for the stiffness observed in natural bone tissue [8, 59].

4.3.8 Mechanical Evaluation of the Composites: Compressive Strength

Fig 4.15 shows the compressive strength measured for the composite to be between 1 and 1.5MPa which is slightly higher than the polymer by 0.3 MPa. In contrast the compressive strength for a real human trabecular bone is between 2 and 12 MPa depending on the type of bone which is slightly higher than the composite. However, it must be noted that trabecular bone is merely the soft bone. The dense or cortical bone possesses an average compressive strength of 125MPa, a value which is 100 times greater than the composite [11, 60, 61]. An interesting observation in fig 4.16 (left) is the behavior of the composite and the polymer at high strains. The material resists break even at 100% strain which practically means the polymer has been deformed into a thin plain sheet and regains at least 95% of its initial shape. Fig 4.16 (right) shows an image of the polymer before and after compression.

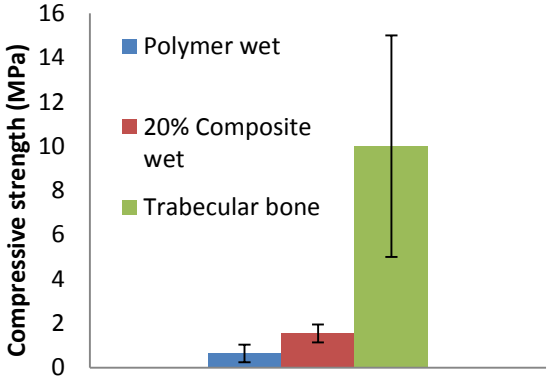

Fig 4.15: Compressive strength of the Polymer, Composite and a rat trabecular bone

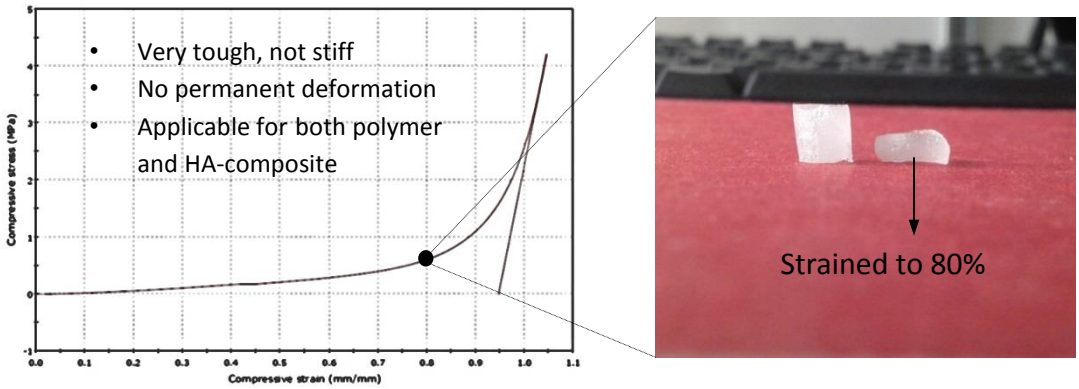

Fig 4.16: (**left**) Stress vs strain plot of the composite. (**right**) Real image showing a normal and 80% strained composite

Results from compression testing and data from literature show that the compressive strength of cortical bone is at least 100 times greater than the composite. According to a series of studies by Fratzl et al., the exemplary mechanical strength and strength to weight ratio of bone can be attributed to its compositional and nanostructural features [9, 59, 62]. Compositionally bone apatite (mineral reinforcement) and collagen type one (protein matrix) deserve equal attention when it comes to stiffness, toughness and fracture resistance of cortical bone. The stiff and brittle mineral phase has major contribution to the stiffness as well as the breaking strain of bone, which translates as higher the mineral content more stiff is bone and susceptible to breaking. On the other hand, the protein collagen and water has an enormous effect on the toughness and flexibility of bone. Collagen has strong hydrogen bonds holding the molecule together and optimum density of fibrillar crosslinks. The crosslinks of the fibers increases the point of contact between them while too many crosslinks makes the matrix more brittle and too little can deteriorate the particle formation. Collagen fibers are arranged in a highly ordered fashion with a well-optimized intrafibrillar crosslinking network[8]. This brings up the next point of nanostructural influence on the mechanical properties of bone. Studies have shown that alteration of this ordered arrangement and crosslink density has negative effects on the mineral particle formation and its size distribution [8, 9, 59]. All the above-mentioned observations suggest that the ordered structure of collagen fibers drive the mineral formation and control over polymorph and size distribution. This in addition to a well-devised mineral composition and polymer chemistry is a strong reason for the influence of nanochemistry and nanostructure on the mechanical properties of bone. In the present case, three major factors can be identified behind the poor mechanical properties of the I_1_20Ca composite.

a. The obvious lack of mineral content in the composite significantly reduces the stiffness and the compressive moduli of the material
b. The composite is made up of amphiphilic molecules cross-linked only at one part of their entire length, which possibly reduces the number of connections between adjacent molecules making the material more flexible and less stiff.
c. The amount of water present in bone is less than 10% of the entire weight which is present as agent to control the crystallinity of apatite as well as partially induce some

flexibility to the entire bone structure [63]. In contrast, the composite possesses a water quantity of nearly 30% present as bound water tightly to the mineral particles or trapped between the pores of the polymeric matrix and CaP particles. The relatively large amount of water is another important factor contributing to the pliability of the composite.

4.4 Controlling CaP Formation at High Precursor Ionic Strength

From the above observations, it is crucial to have high mineral (apatite) content to reach a high compressive strength of the composite. To maximize the mineral content within the composite, a direct approach is to maximize the calcium and phosphate ionic strength of the precursor within the aqueous domains of the polymer. However, at high ionic strengths it was difficult to obtain phase pure apatite due to interference of brushite and monetite. Therefore, it is important to control the type of CaPs to ACP or apatite while attempting to increase the mineral content of the composite. As discussed in section 4.3.5 three specific factors were considered which were suspected to have considerable effect on the polymorph of CaPs formed at high ionic strengths. All composites synthesized for the following studies were prepared from 50wt. % Ca^{2+} precursor solution.

1. Effect of increasing the Ca/P molar ratio in the precursor solution (Ca/P = 3.34)
2. Effect of varying LLC Phase of MF127 to a normal hexagonal phase (H_1)
3. Effect of changing the amphiphile with a shorter chain (DA-ML64 and DA-MP123)

4.4.1 Effect of Varying the Ca/P Molar ratio in Precursor

As discussed in the section 4.3.5, a hypothesis for the formation of brushite and monetite alongside apatite could be attributed to the low Ca/P molar ratio in the precursor solution. At high Ca/P ratio the excess Ca^{2+} ions may act as additives and interfere with CaP crystallization which hinders the formation of brushite or monetite. I_1_50Ca composites were synthesized from a new precursor with an ionic strength of 50wt% Ca^{2+} and a Ca/P ratio of 3.34, double the previous value (1.67). Fig 4.17 shows XRD patterns of composites synthesized from a precursor with Ca/P of 1.67 and 3.34 at 50wt% Ca^2. Bragg peaks corresponding to brushite and monetite (peaks pointed out by arrows in fig 4.17) appear in both composites irrespective of Ca/P ratios.

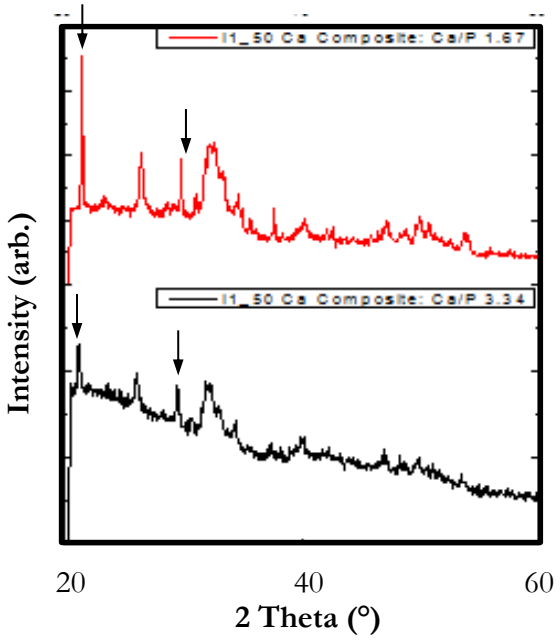

Fig 4.17: XRD diffractograms of I_1_50Ca composites synthesized with precursors having varying Ca/P ratios. Both samples show identical peaks matching with brushite and monetite in addition to broad apatite peaks

Although the peaks corresponding to brushite and monetite are less pronounced in the composite synthesized using a precursor Ca/P ratio of 3.34 when compared to 1.67, the obvious emergence of brushite and monetite peaks irrespective of the Ca/P ratio indicates that the Ca/P molar ratio has little effect on

selective precipitation of ACP or apatite over brushite and monetite. As discussed in section 4.3.5, the burst precipitation of CaP particles is supported by the three dimensional freedom provided by the I_1 phase leading to uncontrolled precipitation.

4.4.2 Effect of Varying the LLC Phase: The H_1 Phase of MF127

To test this theory, hexagonal LLC phases using MF127 and CaP precursor solution were formed to study the effect of LLC phase structure on the polymorph of CaP formed (see table 3.1 for recipe). The SAXS data shown in fig 4.18 (a) confirm the normal hexagonal LLC structure within the polymer and shows the disappearance of the peaks after particle formation. As discussed in section 4.3.1, the SAXS spectra of the composites lack contrast due to high scattering of X-rays by the particles formed. Fig 4.18 (b) shows the predicted model interpreted from SAXS where CaP particles are arranged within the aqueous domains of the H_1 polymer. The diameter of the each aqueous domain of the H_1 polymer (marked as the black circle in fig 4.20) was calculated using simple geometrical assumptions explained in appendix.

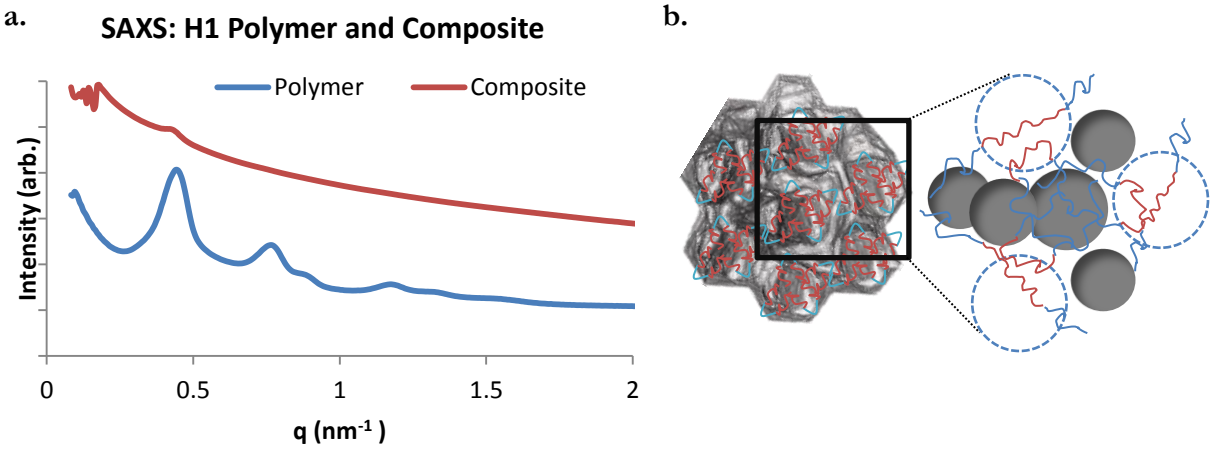

Fig 4.18: (a) SAXS spectra of a H_1 polymer and H_1_50Ca composite showing strong Bragg peaks in the polymer indicating a high degree of long range order in the polymer. **(b)** Predicted model of the cross-linked chains of the polymer and positions of the particles formed within the hexagonal domains

On analyzing the H_1_50Ca composite with XRD, the sample still showed mild traces of monetite (peak indicated with arrow) alongside ACPs, forming within the composite immediately after the reaction (fig 4.19). On aging the composite at room temperature for 2 days, broad apatite peaks become visible with the single monetite peak still present. This suggests that restricting the dimensional freedom of nanoscale aqueous reactors from cubic to hexagonal plays an important role in controlling the CaP polymorph at 50 % wt. Ca^{2+}. A possible hypothesis for this effect is that, normal hexagonal (H_1) liquid crystalline phases provide greater restriction for particle formation due to their degree of freedom being contained in just one dimension (along the length of the cylinder) rather than three. Moreover, presence of an oil phase like butanol further concentrates NH_3 penetration through the aqueous domains which assists favorable ACP formation. This could force the particles to form along the length of the cylinders and not grow in the x or z-plane. The above results suggest the possible role of aqueous domain pore size in a H_1 polymer in controlling the CaP phase formed. The aqueous domain pore size for the H_1 polymer synthesized using DA-MF127 and Ca^{2+} precursor was calculated using equations 3 and 4 (chapter 3, table 3.3) to be 14 nm. Refer appendix for detailed calculation steps.

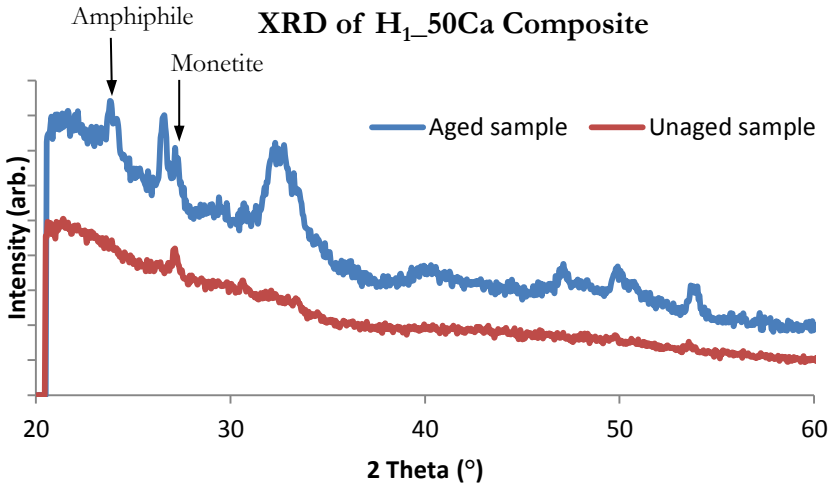

Fig 4.19: XRD patterns of H_1_50Ca composites synthesized from DA-MF127 and 50wt. % Ca^{2+} precursor

To test if lowering the pore size would have a better effect on the CaPs formed, H_1_50Ca composites were synthesized from DA-ML64 and DA-MP123 and evaluated using XRD. The results are presented and discussed in section 4.4.3.

4.4.3 Effect of Varying the Amphiphile: Smaller pore size

The SAXS spectra (appendix) obtained for H_1 polymer and composite synthesized from DA-MP123 and precursor solution confirmed the hexagonal structure while PLM images confirmed the structure retention of polymer and composites synthesized from DA-ML64. The size of the aqueous domains of the H_1 polymer was calculated from equations 3 and 4 and the values are represented in table 4.2

Table 4.2: Details of H_1_50Ca composites synthesized from different amphiphiles of varying chain length.

Sample	Amphiphile: wt. %	50% Ca^{2+} Precursor wt. %	LLC Phase	Aqueous domain diameter (nm)
L1: DA-ML64	60	40	H_1	8.2*
P1: DA-MP123	45	55	H_1	10.3*

*See appendix for calculation procedure

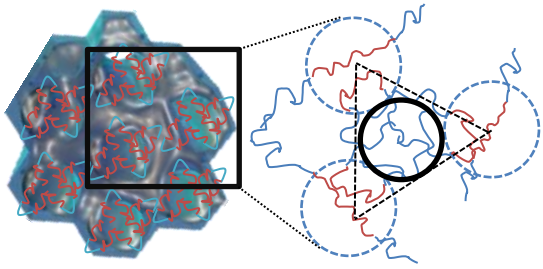

Fig 4.20: The diameter of the marked circle indicates the aqueous domain in question

Composites (L1 and P1 see table 4.2) synthesized from different amphiphiles were analyzed using XRD to determine the type of CaP formed. Fig 4.21 (a) shows the XRD patterns of unaged and aged (RT, 2days) composite of sample L1. The unaged sample show amorphous nature which converts to phase pure, nano-crystalline apatite on aging with no brushite or monetite peaks visible. XRD patterns of sample P1 (fig 4.21, b) also shows pure amorphous character immediately after synthesis and emergence of poorly crystalline apatite peaks on aging at 22° for 1 day. These results suggest that the pore size of the aqueous domain where the mineralization of CaP takes place plays a significant role in forcing the formation of ACPs over other polymorphs such as brushite and monetite. SEM images of both composites (L1 (fig 4.22 a & b) and P1 (fig 4.22 c & d) show a smooth surface with nanosized calcium phosphate particles embedded uniformly within the polymeric matrix.

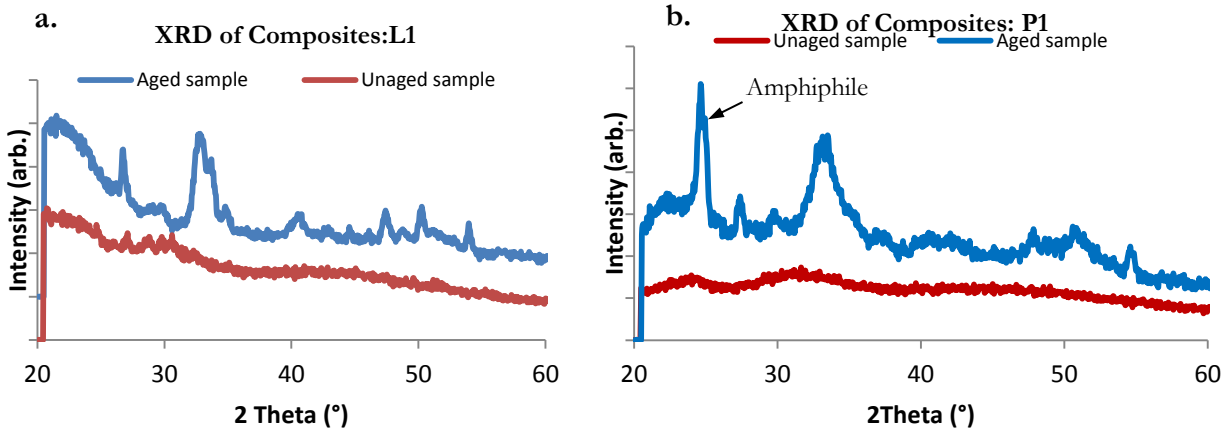

Fig 4.21: XRD patterns of **(a)** unaged and aged H_1_50Ca composites synthesized from DA-L64. **(b)** unaged and aged H_1_50Ca composites synthesized from DA-MP123 both samples show phase pure broad apatite peaks

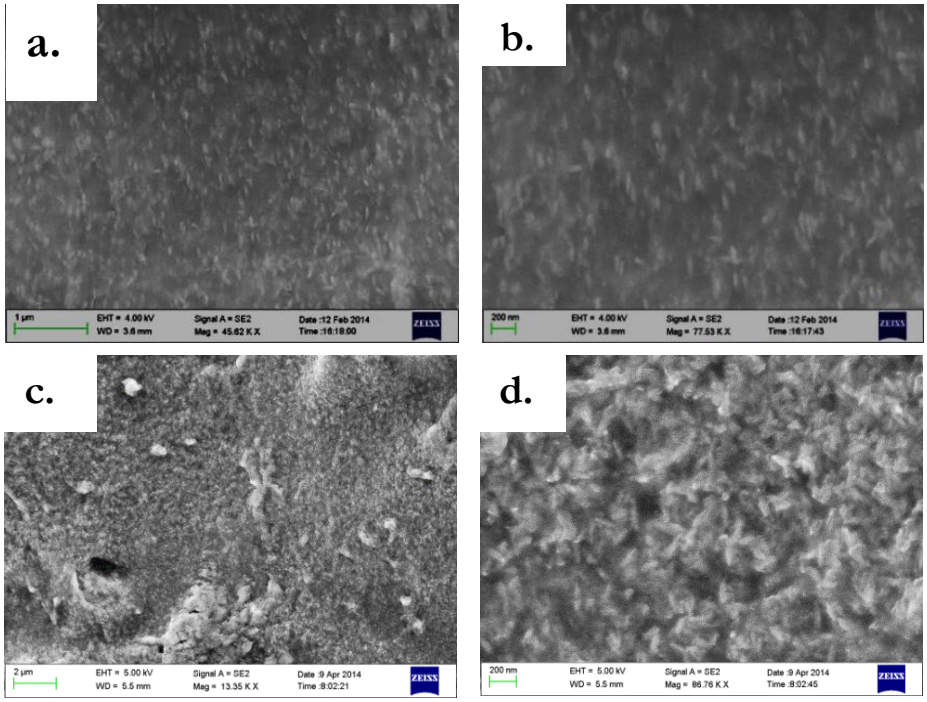

Fig 4.22: **(a and b)** SEM of composite L1 aged. **(c and d)** SEM of composite P1 aged; Both samples show uniform mineralization of the polymer with nanosized CaP particles which were confirmed to be apatite from XRD

Preliminary mechanical evaluations were performed on composite P1 to study if there was an increase in the compressive strength from changing the LLC phase, polymer chain length and presumably a higher mineral content. Fig 4.23 shows the TGA plot of composite P1 which indicates a residual weight of approximately 25% by weight which is slightly higher than the previous composites (I_1_20Ca) but drastically poor when compared to bone. This suggests that a higher ionic strength than 50wt% Ca^{2+} is necessary to increase the mineral content in addition to a higher precursor solution to polymer weight ratio during the synthesis of LLC polymer. The average compressive strength of P1 was 2 MPa while the highest measured value was 4 MPa which was also slightly higher than the earlier composites. The shorter chain length of DA-MP123 when compared to DA-MF127 contributed to the relatively higher stiffness and brittle nature of composite P1. In summary, a higher compressive strength can be achieved by changing synthesis parameters such as increasing the precursor ionic strength, a confined LLC phase, higher precursor to amphiphile ratio in the LLC phase and a polymer of optimal chain length for a good balance between stiffness and toughness.

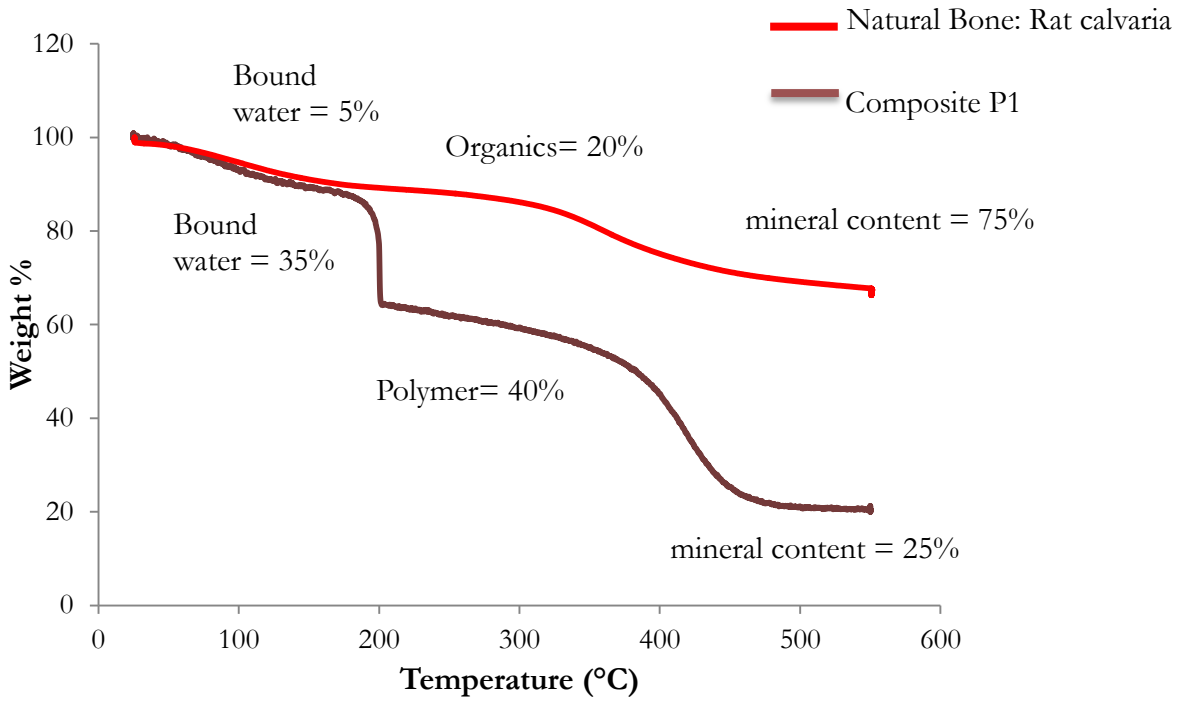

Fig 4.23: TGA plot comparing the compositions of natural bone and the synthetic composite (P1) developed in this thesis

An interesting thought that can be derived from the mechanical studies of the ordered polymers is their strong similarity in compressive strength to human articular cartilage (knee cap) which also has an average value between 1 and 4MPa [64-68]. The pure polymers have potential applications as regenerative scaffolds for cartilage tissue injury from diseases such as osteoarthritis and unnatural cartilage mutilation.

Conclusions and Perspectives

Critical size defects from non-union fractures and bone related diseases like osteoporosis demand interceptive treatment for effective bone healing. Today more than 200 companies around the world produce various orthopedic implants to support the growing clinical demand for rapid healing of bone related issues. However, a major setback with current synthetic implants is their limited lifetime due to mechanical instability, non-adherent fibrous encapsulation, biofilm formation and (or) wear debris. A genuine solution to create an ideal bone implant is to develop a synthetic composite that can mimic the structure, chemistry and mechanics of natural bone.

To mimic the nanostructural order and chemistry of bone, this project aimed at developing a synthetic bone material from ordered lyotropic liquid crystalline (LLC) polymers and bone-like apatite to form an ordered nanocomposite with apatite crystals uniformly located and neatly spaced from each other within the polymer. The rationale behind using LLC phases was due to their ordered and confined aqueous domains where bio-mineralization could be mimicked to form poorly crystalline bone-like apatite. In this study, LLCs were successfully cross-linked to form LLC polymers with cubic and hexagonal geometries possessing long-range order. The nanometric aqueous domains of the polymer functioned as confined reactors for controlled precipitation of bone-like apatite. Results from SAXS suggested that composites retained the meso-ordering, however high scattering of X-rays from the particles reduced the contrast of the bragg peaks. Detailed characterization of the composites using XRD and EDX established that mineralization of bone-like apatite was successful within the polymer. SEM images show well distributed apatite particles separated from each other throughout the whole composite.

Important observations with respect to mineralization were that the cubic phase of polymer failed to control the CaP mineralization at high precursor strengths as acidic polymorphs such as brushite and monetite co-existed with apatite. Controlling the polymorph of CaP to phase pure apatite at high precursor strengths by changing the polymer to a shorter chain and the LLC phase to a hexagonal structure proved as the most important result of this thesis. Dimensional freedom of the LLC phase was observed to play an important role in driving controlled mineralization. Mechanically the composites proved to be soft with an average compressive strength of 2 MPa which is comparable to the human trabecular bone. On comparing the composite with dense cortical bone, literature values suggest that cortical bone is at least 100 times stronger than the composite. Reasons behind the anomaly were the poor mineral content in the composite, inherent pliability of the polymer and relatively high water content contributing for the soft nature of the composites.

In summary, a synthetic composite that mimics the ordered nanostructure and CaP chemistry of natural bone was developed with optimized synthetic parameters and methods. Mechanically, the composite proved soft and pliable, although reasons were identified behind the inconsistencies. This thesis has provided a strong perspective on the future course for the successful development of a composite that can mimic the composition and biomechanics of bone. The first vital step is devise strategies to incorporate higher content of phase pure apatite within the polymer to 50 % by weight for improved compressive strength. Synthetic polymers such as the tri-block copolymers used in this study might face issues with biodegradation and toxic breakdown

products. A solution would be replacing the ordered synthetic matrix with an ordered biomolecular matrix such as lipids or proteins. 3D printing of the composites into shapes that are more distinctive, uniform size and possess microporosity that would favour cell attachment and angiogenesis would prove beneficial when considering clinical applications of the composite. Incorporation of bone healing drugs in the composite and studying the release mechanisms could also prove practical in the clinical scenario. An interesting thought to keep in mind and which requires detailed investigation is the multiple applications the ordered polymers possess as bone scaffolds as well as potential implants for soft tissue regeneration like Achilles heel tendon and articular (knee) cartilage.

Acknowledgments

Chalmers University of Technology, Sweden is acknowledged for the Scholarship support during my MSc studies

I would like to express my gratitude to the below mentioned people;

I am grateful to my loving parents and my adorable girlfriend Ranjani for their strong support and encouragement to live my dreams and reach out to greater heights

My supervisor and examiner Associate Professor, Martin Andersson, for introducing me to the field of biomaterials and giving me the opportunity to develop an exciting biomaterial. Martin, this project has been close to my heart with its wonderful challenges and interesting science. Thank you for your inspiring guidance, educative discussions and moral support that has helped me gain a lot of scientific knowledge. I greatly appreciate the fact that you were always there to answer my questions and help me with my experiments. Thank you for arranging the visit to do interesting experiments at MAX-Lab and at Paris.

My supervisor Wenxiao He (Chlor) for guiding me patiently throughout my project and being always available to answer my doubts and questions. You have been a great source of inspiration for me and I learnt many aspects from you such as doing well-designed experiments, analyzing results and communication of results. Calcium phosphates are really cool!

Dr. Ali Reza Tehrani Bagha for teaching and guiding me with the organic synthesis and TGA measurements. You have imparted me with the knowledge for a significant part of the project. I am sure it would have been difficult to develop the material without your expertise and guidance. Thank you for your valuable scientific inputs and discussions that helped me a lot in designing our materials.

Kurt Löfgren for your help with building the reaction vessel

Dr. Tomás Plivelic and Dr. Christopher Söderberg of MAX-II, Lund for the help with experiments performed at MAX-Lab Lund, Sweden

My group mates at MA Research, Johan Karlsson, Saba Atefyekta, Maria Wallin, Simon Isaksson, Emma Westas, Anna Pekkari and Maria Japlin for your help with my experiments and fun times we had both inside and outside the lab.

Ann Jakobsson for all help with administrative aspects of my stay at TYK

All my friends at TYK, especially my office mates for making my stay at TYK and in Sweden wonderfully memorable

Appendix: Geometrical Calculations of H_1 Polymer

Calculation of parameters d_{hkl}, $2r_{hyp}$, a_1 and a_2 from SAXS data of H_1 polymer synthesized from DA-MP123 and water.

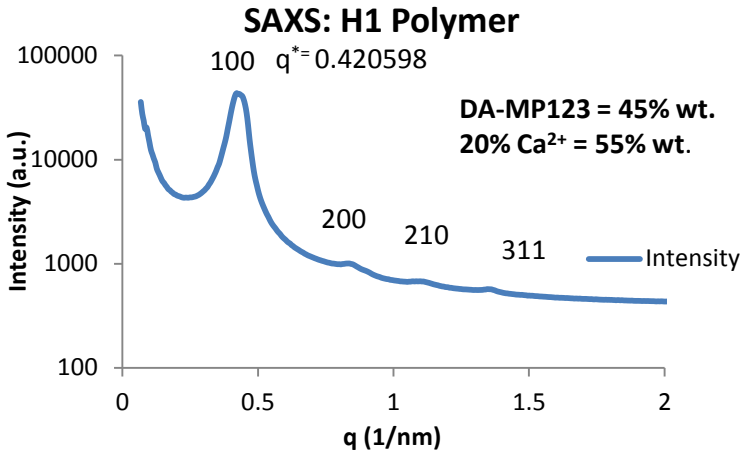

q^* denotes the scattering vector of peak with the highest intensity. Primary peak with miller index (100)

Now, from equation (3), lattice spacing of the cylinders

$$d_{hex} = \frac{2\pi\sqrt{h^2 + k^2 + l^2}}{q_{hkl}} \qquad (3)$$

Substituting q^* and (hkl), d_{hex} = **14.93 nm**

From d_{hex}, $a_1 = 2d_{hex}/3^{1/2}$ = **17.24 nm**

Radius of 1 hydrophobic cylinder =

$$\boldsymbol{R_{hyp} = a_1\left(\frac{\sqrt{3}}{2\pi}f\right)^{1/2}}$$

The parameter f for DA-MP123 = x* Φp = 0.72*0.558 = 0.40 (x and Φp) were taken from [69], see table 3.3, chapter 3 for definitions)

$$R_{hyp} = 17.24\left(\frac{\sqrt{3}}{2\pi}0.40\right)^{1/2} = \boldsymbol{5.78nm}$$

Therefore, the predicted model of the structure would be:

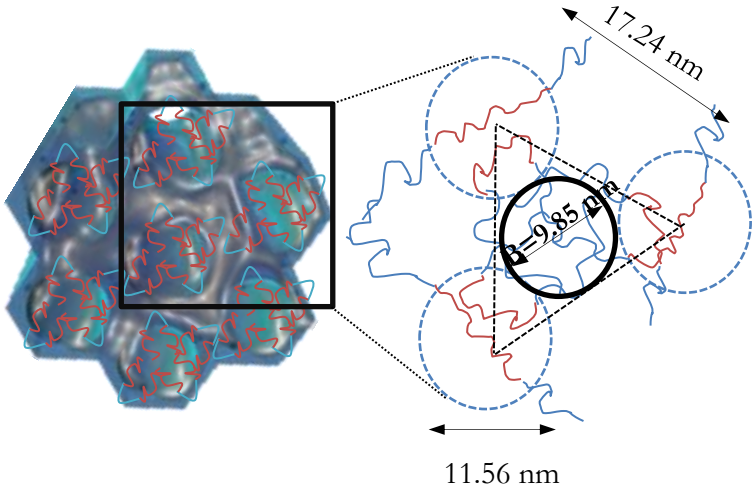

From the derived values of the geometrical Fig, parameter **B** can be determined which gives the pore size of aqueous domain (assuming each domain to be sphere within an equilateral triangle of side 17.24 nm)

By subtracting the area of the 3 sectors of the surrounding hydrophobic spheres from the area of the equilateral triangle, we get the area and diameter of the inner circle **B= 9.85 nm**.

Note: This value is not the exact size of the water domain as the above method of calculation is only an approximation. **The error factor could be ± 2nm**

References

1. Porter, J.R., T.T. Ruckh, and K.C. Popat, *Bone tissue engineering: a review in bone biomimetics and drug delivery strategies.* Biotechnol Prog, 2009. **25**(6): p. 1539-60.
2. Langer, R. and J.P. Vacanti, *Tissue Engineering.* Science, 1993. **260**(5110): p. 920-926.
3. Dumitrescu, A.L., *Bone Grafts and Bone Graft Substitutes in Periodontal Therapy.* 2011: p. 73-144.
4. Stevens, M.M., *Biomaterials for bone tissue engineering.* Materials Today, 2008. **11**(5): p. 18-25.
5. Reichert, J.C. and D.W. Hutmacher, *Bone Tissue Engineering*, in *Tissue Engineering*, N. Pallua and C.V. Suscheck, Editors. 2011, Springer Berlin Heidelberg. p. 431-456.
6. Ramiah, R.D., et al., *Ten-year life expectancy after primary total hip replacement.* Journal of Bone & Joint Surgery, British Volume, 2007. **89-B**(10): p. 1299-1302.
7. Alexander, B., et al., *The nanometre-scale physiology of bone: steric modelling and scanning transmission electron microscopy of collagen-mineral structure.* J R Soc Interface, 2012. **9**(73): p. 1774-86.
8. Fratzl, P., et al., *Structure and mechanical quality of the collagen?mineral nano-composite in bone.* Journal of Materials Chemistry, 2004. **14**(14): p. 2115.
9. Rho, J.-Y., L. Kuhn-Spearing, and P. Zioupos, *Mechanical properties and the hierarchical structure of bone.* Medical Engineering & Physics, 1998. **20**(2): p. 92-102.
10. Fratzl, P., et al., *Nucleation and growth of mineral crystals in bone studied by small-angle X-ray scattering.* Calcified Tissue International, 1991. **48**(6): p. 407-413.
11. Fu, Q., et al., *Bioactive glass scaffolds for bone tissue engineering: state of the art and future perspectives.* Materials Science and Engineering: C, 2011. **31**(7): p. 1245-1256.
12. Salgado, A.J., O.P. Coutinho, and R.L. Reis, *Bone tissue engineering: state of the art and future trends.* Macromol Biosci, 2004. **4**(8): p. 743-65.
13. Mann, S., *Mineralization in biological systems*, in *Inorganic Elements in Biochemistry*. 1983, Springer Berlin Heidelberg. p. 125-174.
14. Nudelman, F. and N.A. Sommerdijk, *Biomineralization as an inspiration for materials chemistry.* Angew Chem Int Ed Engl, 2012. **51**(27): p. 6582-96.
15. Mann, S. and G.A. Ozin, *Synthesis of inorganic materials with complex form.* Nature, 1996. **382**(6589): p. 313-318.
16. Mann, S., *Crystallization at inorganic-organic interfaces: Biominerals.* Science, 1993. **261**(5126): p. 1286.
17. Sarikaya, M., *Biomimetics: Materials fabrication through biology.* Proceedings of the National Academy of Sciences, 1999. **96**(25): p. 14183-14185.
18. Yang, H., N. Coombs, and G.A. Ozin, *Morphogenesis of shapes and surface patterns in mesoporous silica.* Nature, 1997. **386**(6626): p. 692-695.
19. Moreau, J.W., et al., *Extracellular Proteins Limit the Dispersal of Biogenic Nanoparticles.* Science, 2007. **316**(5831): p. 1600-1603.
20. Cha, J.N., et al., *Biomimetic synthesis of ordered silica structures mediated by block copolypeptides.* Nature, 2000. **403**(6767): p. 289-92.
21. He, W., et al., *Formation of Bone-like Nanocrystalline Apatite Using Self-Assembled Liquid Crystals.* Chemistry of Materials, 2012. **24**(5): p. 892-902.
22. Wenxiao, H., et al., *Osteogenesis-inducing calcium phosphate nanoparticle precursors applied to titanium surfaces.* Biomedical Materials, 2013. **8**(3): p. 035007.
23. Holmberg, K., et al., *Phase Behaviour of Concentrated Surfactant Systems*, in *Surfactants and Polymers in Aqueous Solution*. 2002, John Wiley & Sons, Ltd. p. 67-96.

24. Alexandridis, P., *Amphiphilic copolymers and their applications.* Current Opinion in Colloid & Interface Science, 1996. **1**(4): p. 490-501.
25. Singh V, S.H., Veerma R, Javed A, Singh M, *Topical non steroidal anti inflammatory drug* Asian J Pharm 2013. **7**: p. 1-7.
26. Malmsten, M., *Soft drug delivery systems.* Soft Matter, 2006. **2**(9): p. 760-769.
27. Harmankaya, N., et al., *Raloxifene and alendronate containing thin mesoporous titanium oxide films improve implant fixation to bone.* Acta Biomaterialia, 2013. **9**(6): p. 7064-7073.
28. Ehlert, N., et al., *Mesoporous silica coatings for controlled release of the antibiotic ciprofloxacin from implants.* Journal of Materials Chemistry, 2011. **21**(3): p. 752-760.
29. Kjellin, P. and M. Andersson, *Synthetic nano-sized crystalline calcium phosphate and method of production*, 2012, Google Patents.
30. Yang, P., et al., *Generalized syntheses of large-pore mesoporous metal oxides with semicrystalline frameworks.* Nature, 1998. **396**(6707): p. 152-155.
31. Alexandridis, P., *Poly(ethylene oxide)/poly(propylene oxide) block copolymer surfactants.* Current Opinion in Colloid & Interface Science, 1997. **2**(5): p. 478-489.
32. Holmqvist, P., P. Alexandridis, and B. Lindman, *Phase Behavior and Structure of Ternary Amphiphilic Block Copolymer−Alkanol−Water Systems: Comparison of Poly(ethylene oxide)/Poly(propylene oxide) to Poly(ethylene oxide)/Poly(tetrahydrofuran) Copolymers.* Langmuir, 1997. **13**(9): p. 2471-2479.
33. Wanka, G., H. Hoffmann, and W. Ulbricht, *Phase Diagrams and Aggregation Behavior of Poly(oxyethylene)-Poly(oxypropylene)-Poly(oxyethylene) Triblock Copolymers in Aqueous Solutions.* Macromolecules, 1994. **27**(15): p. 4145-4159.
34. Dorozhkin, S.V. and M. Epple, *Biological and Medical Significance of Calcium Phosphates.* Angewandte Chemie International Edition, 2002. **41**(17): p. 3130-3146.
35. Dorozhkin, S., *Calcium Orthophosphates in Nature, Biology and Medicine.* Materials, 2009. **2**(2): p. 399-498.
36. Wang, L. and G.H. Nancollas, *Calcium Orthophosphates: Crystallization and Dissolution.* Chemical Reviews, 2008. **108**(11): p. 4628-4669.
37. Olszta, M.J., et al., *Bone structure and formation: A new perspective.* Materials Science and Engineering: R: Reports, 2007. **58**(3-5): p. 77-116.
38. Bone Biology and Mechanics Lab, I.U.-P.U.a.I., *http://www.iupui.edu/~bbml/boneintro.shtml*.
39. Posner, A.S. and F. Betts, *Synthetic amorphous calcium phosphate and its relation to bone mineral structure.* Accounts of Chemical Research, 1975. **8**(8): p. 273-281.
40. Mahamid, J., et al., *Amorphous calcium phosphate is a major component of the forming fin bones of zebrafish: Indications for an amorphous precursor phase.* Proc Natl Acad Sci U S A, 2008. **105**(35): p. 12748-53.
41. Combes, C. and C. Rey, *Amorphous calcium phosphates: synthesis, properties and uses in biomaterials.* Acta Biomater, 2010. **6**(9): p. 3362-78.
42. Politi, Y., et al., *Sea urchin spine calcite forms via a transient amorphous calcium carbonate phase.* Science, 2004. **306**(5699): p. 1161-4.
43. Boskey, A.L. and A.S. Posner, *Conversion of amorphous calcium phosphate to microcrystalline hydroxyapatite. A pH-dependent, solution-mediated, solid-solid conversion.* The Journal of Physical Chemistry, 1973. **77**(19): p. 2313-2317.
44. Li, Y. and W. Weng, *In vitro synthesis and characterization of amorphous calcium phosphates with various Ca/P atomic ratios.* J Mater Sci Mater Med, 2007. **18**(12): p. 2303-8.

45. Hentze, H.P., et al., *Lyotropic Mesophases of Poly(ethylene oxide)-b-poly(butadiene) Diblock Copolymers and Their Cross-Linking To Generate Ordered Gels.* Macromolecules, 1999. **32**(18): p. 5803-5809.
46. Gin, D.L., et al., *Polymerized Lyotropic Liquid Crystal Assemblies for Membrane Applications.* Macromolecular Rapid Communications, 2008. **29**(5): p. 367-389.
47. Lee, D.-I., et al., *Synthesis and characterization of TRITON™ X-based surfactants with carboxylic or amino groups in the oxyethylene chain end.* Journal of Applied Polymer Science, 2007. **104**(1): p. 162-170.
48. Summers, M. and J. Eastoe, *Applications of polymerizable surfactants.* Advances in Colloid and Interface Science, 2003. **100-102**: p. 137-152.
49. Holmqvist, P., P. Alexandridis, and B. Lindman, *Modification of the Microstructure in Block Copolymer−Water−"Oil" Systems by Varying the Copolymer Composition and the "Oil" Type: Small-Angle X-ray Scattering and Deuterium-NMR Investigation.* The Journal of Physical Chemistry B, 1998. **102**(7): p. 1149-1158.
50. Alexandridis, P., U. Olsson, and B. Lindman, *Self-Assembly of Amphiphilic Block Copolymers: The (EO)13(PO)30(EO)13-Water-p-Xylene System.* Macromolecules, 1995. **28**(23): p. 7700-7710.
51. Ivanova, R., B. Lindman, and P. Alexandridis, *Evolution in Structural Polymorphism of Pluronic F127 Poly(ethylene oxide)−Poly(propylene oxide) Block Copolymer in Ternary Systems with Water and Pharmaceutically Acceptable Organic Solvents: From "Glycols" to "Oils"†.* Langmuir, 2000. **16**(23): p. 9058-9069.
52. Materials Measurement Labaratory, N.I.o.S.a.T., *Dimensional Metrology for Nanoscale Patterns.*
53. Wang, Z., et al., *Microstructure and rheological properties of liquid crystallines formed in Brij 97/water/IPM system.* Journal of Colloid and Interface Science, 2006. **297**(2): p. 813-818.
54. Wang, J. and X. Yu, *Preparation, characterization and in vitro analysis of novel structured nanofibrous scaffolds for bone tissue engineering.* Acta Biomater, 2010. **6**(8): p. 3004-12.
55. Tas, A.C. and P. Brown, *Granules of Brushite and Octacalcium Phosphate from Marble.* Journal of the American Ceramic Society, 2011. **94**(11): p. 3722-3726.
56. Mandel, S. and A.C. Tas, *Brushite (CaHPO4·2H2O) to octacalcium phosphate (Ca8(HPO4)2(PO4)4·5H2O) transformation in DMEM solutions at 36.5°C.* Materials Science and Engineering: C, 2010. **30**(2): p. 245-254.
57. Tang, R., et al., *Dual roles of brushite crystals in calcium oxalate crystallization provide physicochemical mechanisms underlying renal stone formation.* Kidney Int, 2006. **70**(1): p. 71-78.
58. Somrani, S., et al., *Physico-chemical and thermochemical studies of the hydrolytic conversion of amorphous tricalcium phosphate into apatite.* Journal of Solid State Chemistry, 2005. **178**(5): p. 1337-1348.
59. Ji, B. and H. Gao, *Mechanical properties of nanostructure of biological materials.* Journal of the Mechanics and Physics of Solids, 2004. **52**(9): p. 1963-1990.
60. Beaupied, H., E. Lespessailles, and C.L. Benhamou, *Evaluation of macrostructural bone biomechanics.* Joint Bone Spine, 2007. **74**(3): p. 233-9.
61. Røhl, L., et al., *Tensile and compressive properties of cancellous bone.* Journal of Biomechanics, 1991. **24**(12): p. 1143-1149.
62. Gao, H., et al., *Materials become insensitive to flaws at nanoscale: lessons from nature.* Proc Natl Acad Sci U S A, 2003. **100**(10): p. 5597-600.
63. Wang, Y., et al., *Water-mediated structuring of bone apatite.* Nat Mater, 2013. **12**(12): p. 1144-1153.

64. Shah, R.N., et al., *Supramolecular design of self-assembling nanofibers for cartilage regeneration.* Proc Natl Acad Sci U S A, 2010. **107**(8): p. 3293-8.
65. Kloxin, A.M., et al., *Photodegradable hydrogels for dynamic tuning of physical and chemical properties.* Science, 2009. **324**(5923): p. 59-63.
66. Keeney, M., J.H. Lai, and F. Yang, *Recent progress in cartilage tissue engineering.* Curr Opin Biotechnol, 2011. **22**(5): p. 734-40.
67. Buckwalter, J.A., A.J. Mankin Hj Fau - Grodzinsky, and A.J. Grodzinsky, *Articular cartilage and osteoarthritis.* (0065-6895 (Print)).
68. Boschetti, F., et al., *Biomechanical properties of human articular cartilage under compressive loads.* Biorheology, 2004. **41**(3): p. 159-166.
69. Soni, S.S., et al., *Quantitative SAXS Analysis of the P123/Water/Ethanol Ternary Phase Diagram.* The Journal of Physical Chemistry B, 2006. **110**(31): p. 15157-15165.